TÉCNICO LISBOA

Synthesis and characterization of membranes of Hemodialysis

Jennifer Gildo Alberto

Thesis to obtain the Master of Science Degree in

Chemical Engineering

Supervisors: Prof. Dr. Maria Norberta Neves Correia de Pinho

Dr. María Teresa Viciosa Plaza

Examination comitte

Chairperson: Prof. Maria Filipa Gomes Ribeiro

Members of Comitte: Prof. Maria Madalena Dionísio Andrade

Prof. Luis Miguel Minhalma

Dr. María Teresa Viciosa Plaza

June 2023

Acknowledgments

My first gratitude goes to God, who has illuminated my way, given me strength, and allowed me to continue this road despite immense adversity.

Special gratitude goes to my dear parents Marcelino Gildo Alberto and Célia Nascimento Nhapulo to guiding me, my sister Marcela Gildo Alberto and my brother Edilson Gildo Alberto to give me moral support. My Portugal family, uncle João Gonçalves and auntie Maria de Fátima nunes.

A particular gratitude to my advisors, Prof. Maria Norberta de Pinho and Maria Teresa Viciosa, who have been extremely helpful and supportive from the beginning to the finish of my dissertation.

A special gratitude to Miguel da Silva for accompanying, supporting, and guiding me in the Laboratory of Membrane Processes, during the experimental phase of my research.

Gratitute to Prof.Dr. Madalena Dionisio for the facilities with the calorimetric and dielectric equipment.

Finally, I want to thank my friends to always support me and to making part of my good and bad moments.

Abstract

Mixed matrix membranes of cellulose acetate (CA) and Silica (CA/SiO_2) were synthetized by coupling the wet phase inversion technique and the sol-gel method. Other set of CA based membranes were synthesized by direct mixing of the Metal Organic Framework (MOF) - UiO66 - in the casting solution of the CA and CA/SiO_2 membranes (CA_UiO66 and CA/SiO_2_UiO66). CA and CA/SiO_2 membranes were subjected to a pos-treatment with solutions of glycerol (20%) (G20) or glycerol (20%) and triton-X-100 (4%) (GT).

The physical and chemical properties of the membranes were investigated by Differential Scanning Calorimetry (DSC) and Dielectric Relaxation Spectroscopy (DRS). The former allowed determining parameters such as the crystallinity degree and the glass transition temperature (T_g). On the other hand, DRS was used to analyze the molecular dynamics of each CA based membranes in the sub-T_g temperature region. The different relaxation processes detected were interpreted considering the interactions of membranes with water, glycerol, and triton-X-100.

The membranes selective performance was correlated with the characterization parameters: hydraulic permeabilities, Molecular Weight Cut-Off (MWCO), and apparent rejection coefficients to NaCl, Na_2SO_4, urea, and P-Cresyl sulphate (PCs) and P-Cresyl sulphate with Bovine Serum Albumin (BSA).

Resumo

Membranas híbridas assimétricas de acetato de celulose (CA) e sílica (CA/SiO_2) foram sintetizadas por acoplamento entre a técnica de inversão de fase húmida e o método sol-gel. Outro conjunto de membranas foi sintetizado por mistura direta de uma estrutura metal-orgânica UiO66, nas soluções percussoras das membranas CA/SiO_2.

As membranas CA e CA/SiO_2 foram submetidas a pós-tratamento com as seguintes soluções aquosas de glicerol (20%) (G20) e com tritão-X-100(4%) e com glicerol (20%) (GT). Após a síntese das membranas, as propriedades físico-químicas das membranas foram investigadas por Calorimetria Diferencial de Varrimento (DSC) e Espectroscopia de relaxamento dielétrico (DRS). A técnica da DSC permitiu determinar parâmetros como o grau de cristalinidade e a temperatura de transição vítrea (T_g). Por outro lado, a técnica de DRS foi utilizada para analisar a dinâmica molecular de cada uma das membranas baseadas em CA na região de temperatura acima da T_g. Os diferentes processos de relaxamento detetados foram interpretados considerando as interações da matriz CA e CA/SiO_2 com água, glicerol e tritão-X-100.

A permeação seletiva foi correlacionada com parâmetros de caracterização das membranas: permeabilidades hidráulicas, *cut-off* molecular e coeficientes de rejeição aparente para NaCl, Na_2SO_4, ureia, sulfato de p-cresilo e sulfato de p-cresilo e Albumina.

Table of Contents

Abbreviation list

CKD - chronic kidney disease

ESRD - End stage renal disease

PBUTs - Protein-bound uremic toxins

MWCO - Molecular weight cut-off

ΔP_t - Transmembrane pressure

L_p - Hydraulic permeability

f - apparent rejection coefficient

J_w - Pure water permeate mass flux

J_p - Permeate mass flux

PEG - Polyethylene glycol

HAS - Human serum albumin

BSA -Bovine serum albumin

TOC - Total organic carbon

TEOS – Tetraethoxysilan

PCs - P-Cresyl sulfate

DRS - Dielectric relaxation spectroscopy

DSC - Differential scanning calorimetry

HD - Hemodialysis

T_g - Glass transition temperature

MOF- Metal organic framework

UiO66- prototypical and stable Metal Organic Framework

CA - cellulose acetate

CA/SiO_2 –Hybrid Cellulose acetate membrane with Silica precursor

CA_UiO66-Cellulose acetate membrane with MOF

CA/SiO_2_UiO66 – Hybrid Cellulose acetate membrane with silica precursor and MOF

CA_G20 – Post-treated cellulose acetate membrane with 20% of glycerol

CA_GT – Post-treated cellulose acetate membrane with 20% of glycerol and 4% of Triton-X solution.

CA/SiO_2_G20-Post-treated hybrid membrane with 20% of glycerol solution

CA/SiO_2_GT- Post-treated hybrid membrane with 20% of glycerol and 4% of Triton-X solution

ε* - Complex permittivity

ε´ - Real part of complex permittivity

ε´´ - Imaginary part of complex permittivity

M* - Dielectric modulus

M´´ - Imaginary part of dielectric modulus

List of Tables

List of figures

1.Introduction

Chronic kidney disease (CKD) has been one of the biggest concerns in the medical world in recent years and is expected to rise over the next decades [1]. This disease affects 11-13% of the population worldwide [2].

This disease is related to the accumulation of uremic toxics that can lead to end stage renal disease (ESRD). Patients that reach the ESRD-stage, may be subjected to a renal replacement therapy (Hemodialysis) or transplantation. Transplantation depends on finding compatible healthy kidney donors and the procedure may put the patient under various risks. Hemodialysis (HD) has been the most viable route for this type of disease. Hemodialysis is the renal replacement therapy where blood purification is employed to take out metabolic leftovers that accumulate in the blood of patients with ESRD. Semi-permeable membranes are arranged in a compact fashion known as membrane module it provides the setup of channels for the counter-current flows of blood and dialysate fluids (Figure 1). A membrane is the core component of the HD machine, for the extracorporeal treatment [1,3].

Toxin elimination from blood can reduce problems and increase survival time in dialysis patients. However, Protein-Bound Uremic Toxins (PBUTs) are difficult to eliminate during conventional hemodialysis (HD) since they bind preferentially to proteins. Protein-bound uremic toxins clearances would be improved if there are binding sites competitive to the ones of the plasma proteins [4].

According to European Uremic Toxin work group (EUTox), the uremic toxins can be classified and described in terms of molecular weight and relative affinity for protein (Table 1)[5,6].

Table 1- Different classes of uremic toxins, as proposed by the European Uremic Toxin work group (EUTox). adapted from [5,6].

Class of molecules	Mw range	Percentage of identified molecules (%)	Prototype	MWprototype
Small water-soluble compounds	<500 Da	46	Urea	60 Da
Protein-bound uremic toxins	And >66500 when bound to albumin	26	Indoxyl sulfate, P_Cresyl sulfate	213 Da 108 Da
Middle molecules	>= 500 Da	28	β_2_microglobulin	11 818 Da

The membrane used in hemodialysis is critical to its success. A membrane is defined as a permselective barrier, or interphase, that forms the boundary between two separate gaseous or liquid mixes where mass exchanges of solute and solvent molecules occur at different rates due to a driving force.

Biocompatibility, good balance in water and solute permeability, sufficient mechanical strength at varied trans-membrane pressures, sterilizing capabilities, and low cost are all characteristics for a high-performance membrane (HPM) [3,7].

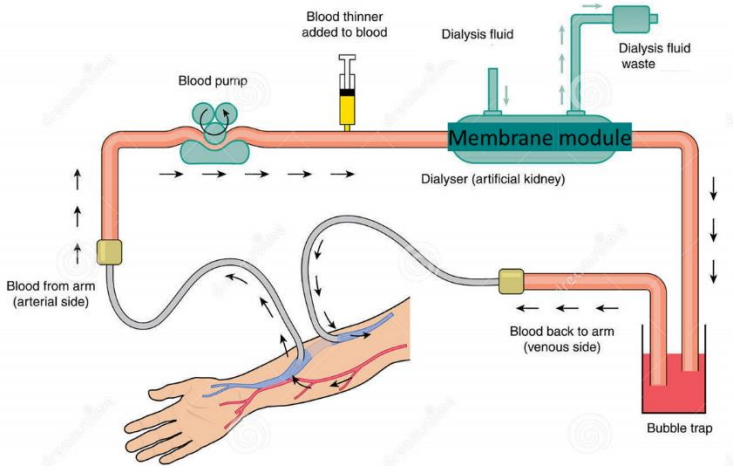

Figure 1- Representation of the extracorporeal blood circuit in hemodialysis (adapted from 8]).

1.1 Separation processes with membranes

Membranes permeate selectively, thus different solute species are permeated and able to pass the interphase while others are kept due to their structure or size [9].

Membrane separation is often accomplished at room temperature, allowing sensitive solutions to be treated without having their chemical structure altered or harmed [10,11].

The most common membrane separation processes are those where the driving force of transport is the difference hydrostatic pressure stablished between feed and the permeate channel. Pressure-driven membrane processes include tangential Microfiltration (MF), Ultrafiltration (UF), Nanofiltration (NF), and Reverse Osmosis (RO) [12].

Membranes separation processes can operate in crossflow mode, and dead-end mode. In crossflow mode the fluid circulates tangentially to the membrane surface, and dead-end, the feed circulates perpendicular to the membrane [9,10]. Crossflow filtration is employed to reduce concentration polarization, which is a precursor to membrane fouling. This is especially important for large-scale water treatment. The dead-end type is frequently utilized in microfiltration for the retention of suspended particles and cake formation [13,14] (Figure 2). Due to orientation of the feed flow, the crossflow type is less prone to fouling than dead-end filtration [15,16].

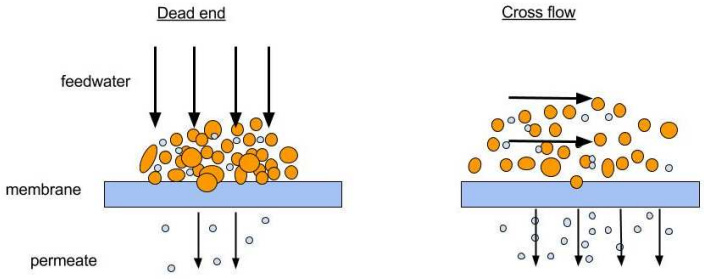

Figure 2- Representation of Dead end and cross flow filtration [17].

This project is focused on Ultrafiltration using crossflow filtration with pressure as a driving force.

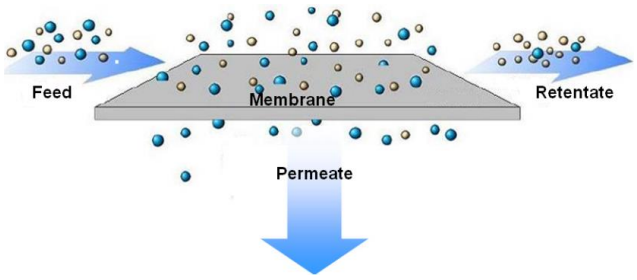

Figure 3- Schematic representation of Separation process by membrane [18].

In this separation process (**Erro! A origem da referência não foi encontrada.**) the feed tangentially circulates at the membrane and due to the transmembrane pressure difference provided, the feed current separates into two: permeate current that crosses the membrane and concentrate/retentate current that contains the fraction of solution rejected by the membrane.

1.2 Membrane structure and preparation

The structure of the membranes depends on the preparation procedure. to facilitate the attainment of its objective [19]. In Figure 4, depicts the many matrials, architeres ,and configurations considered while creating membranes.

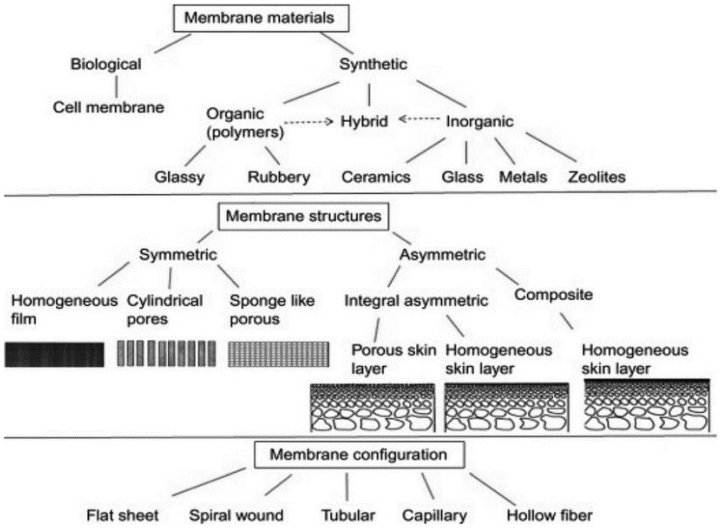

Figure 4- Classification of membranes based on materials of construction, structural attributes, and configuration [19].

Membrane structures are divided into two types: symmetric and asymmetric membranes. The symmetric membrane (usually used in Microfiltration) has a consistent cross-section structure that might be microporous or dense along all their thickness [19] (Figure 5). Regarding asymmetric membranes, they have layer supported by porous. Asymmetric membranes (Figure 6)are used in Nanofiltration, Ultrafiltration, Reverse osmosis, and gas separation processes. Moreover, the asymmetric membranes have two subgroups: Integral Asymmetric and thin-film composite membrane (Figure 7). In the Integral asymmetric the dense layer and the porous sublayer use the same material, while Composite asymmetric membranes are the result of a dense selective layer being deposited upon a porous substrate made of a different polymeric substance [19, 20].

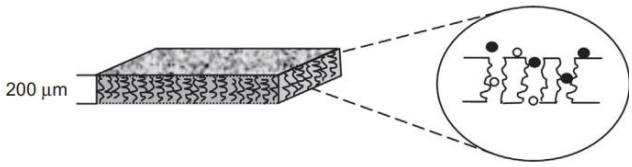

Figure 5- Scheme and cross-section diagram of a symmetric membrane [20].

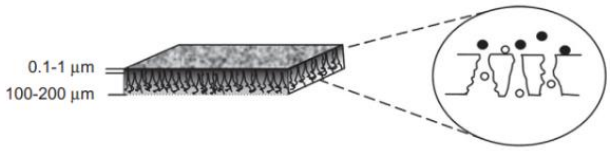

Figure 6- Scheme and cross-section diagram of an asymmetric membrane [20].

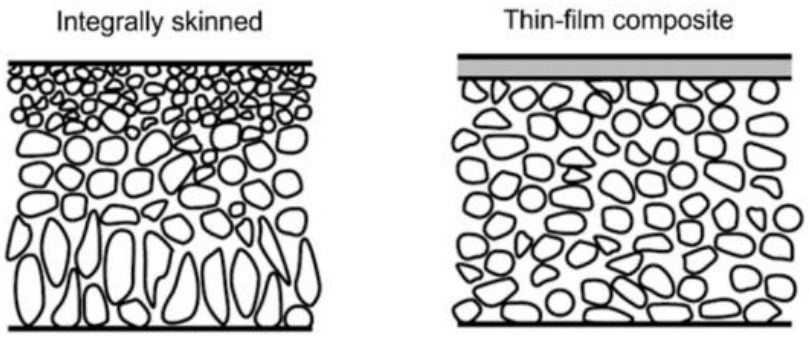

Figure 7- Cross-section representation of integrally skinned (integrally asymmetric) and Thin-film composite membranes [21].

1.2.1 Wet-Phase inversion method

Cellulose acetate (CA) membranes were development in 1960s by Loeb and Sourirajan [22] for desalination of seawater in order to obtain membranes appropriate for industrial applications due to their chemical and mechanical strength and high permeability. These membranes are synthesized by the method of phase inversion, which gives them an asymmetric structure.

Phase inversion is a method based on converting a polymer from a liquid to a solid. This method was created using Loeb and Sourirejan method by combining polymer, solvent, and nonsolvent [22]. This method is used to produce a skinned asymmetric membrane like the membranes used in this work.

As mentioned before, these membranes have two layers: top skin layer and a porous sublayer. The top layer controls the membrane's selective permeability capabilities, whereas the porous sublayer just provides mechanical support.

An appropriate solvent is used to dissolve the polymer. The polymer solution that results is cast on an appropriate substrate and immersed in a coagulation bath containing a nonsolvent (often water).

A ternary phase diagram can be used to explain how this method works with polymer, solvent, and non-solvent system (Figure 8) [23,24]. The path from A to D represents the whole

phase inversion process of a polymeric solution. The solvent diffuses out of the polymeric solution after immersion in a nonsolvent coagulation bath, while the nonsolvent diffuses into the solution. The polymer concentration at the contact rises, and precipitation begins (as illustrated by point B-precipitation). The solidification of the polymer-rich phase (point C) would arise from the replacement of solvent with nonsolvent.

Thus, solvent/nonsolvent exchange would cause the polymer-rich phase to shrink, eventually leading to point D, where two phases (solid and liquid) are in equilibrium. Point S represents the solid (polymer-rich) phase that forms the membrane structure, and point L represents the liquid (polymer-poor) phase that comprises the membrane holes filled with nonsolvent [24].

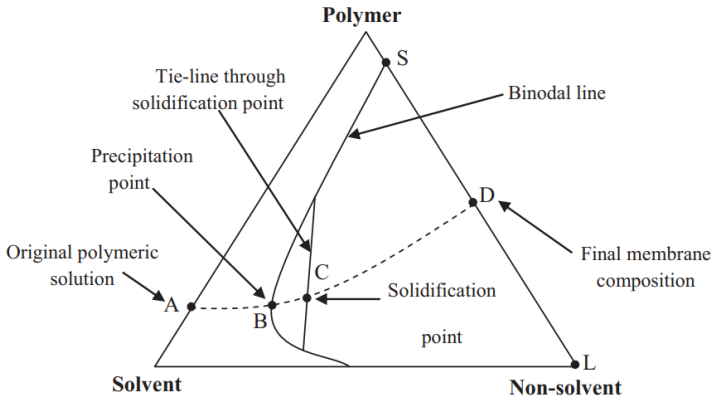

Figure 8- Schematic ternary phase diagram for polymer/solvent/nonsolvent systems [23,24]

1.2.2. Phase inversion coupled with Sol-gel method.

The sol-gel approach is a versatile strategy for producing functional inorganic and hybrid materials that allows for greater control over the organization and composition of the material.

Aqueous solutions and silicon alkoxides, commonly tetraethyl orthosilicate (TEOS) are the common precursors utilized in the approach of Sol-gel technique, which result in a polymer/silica

matrix following hydrolysis/condensation, with good thermal stability, hydrophilicity, and flexibility [25,26].

Since the silicon alkoxides are not sensitive to hydrolysis an acid or a base catalyst must be added to boost the rates of hydrolysis and condensation. Thus, there are 3 reactions that represent the hydrolysis and condensation of silicon alkoxides in t sol-gel technique. First, the hydrolysis happens and allows substitution of alkoxide groups with hydroxyl groups (Equation 1) Further condensation operations involving silanol groups produce siloxane bonds, and the byproducts are alcohols (Equation 2) or water (Equation 3)[27].

$$\equiv Si - OR + H_2O \leftrightarrow \equiv Si - OH + ROH \qquad \text{Equation 1}$$

$$\equiv Si - OR + OR - Si \equiv \leftrightarrow \equiv Si - O - Si \equiv + ROH \qquad \text{Equation 2}$$

$$\equiv Si - OR + HO - Si \equiv \leftrightarrow \equiv Si - O - Si \equiv + H_2O \qquad \text{Equation 3}$$

2.Literature review

2.1. Mixed Matrix Membranes (MMMs)

The synthesis of Mixed Matrix Membranes (MMMs) is made by incorporating in a polymeric matrix an organic/inorganic particle [28]. The incorporation of these filler particles into the polymeric matrix combines the high permeability and separation efficiency of sieving materials like zeolites, MOFs, or other nanoparticles with the processing capabilities and mechanical properties of glassy polymers [29,30]. Nonetheless, it is vital to verify that the materials used as filler particles are compatible with the polymeric matrix so that particle clusters do not develop in the matrix and there are no flaws at the polymer-particle interface due to poor adherence of these particles to the matrix .Thus, optimizing MMMs entails homogeneous dispersion of filler material particles, which reduces incompatibility between them and the polymeric matrix [31,32].

MMMs have been used in healthcare applications such as for the removal of uremic toxins attached to proteins in HD or to remove urea from wasted dialysis fluid, and in MMMs in water treatment MOFs are used as filler particles [33,34]

2.2. Removal of Protein-Bound Uremic Toxin (PBUT) from Human Serum Albumin

These are a heterogeneous group of organic compounds with intrinsic biological activities, many of which are too large to be filtered and/or are protein bound. The renal excretion of protein-bound toxins depends largely on active tubular secretion, which shifts the binding and allows for active secretion of the free fraction.

The uremic toxins, including, indoxyl sulfate p-cresyl sulfate, and hippuric acid (PTUBs) primarily bind to the human serum albumin (HSA) in human blood[35] and they have an aromatic moiety and an ionic functional group, allowing electrostatic and/or van der Waals forces to attach to numerous adsorption sites on HAS [36].So these interactions prevent the efficient removal of PBUTs through conventional extracorporeal renal replacement therapies, such as a hemodialysis.

In general, protein-bound uremic toxins (PBUTs) have MWs smaller than 500 Da but are difficult to remove through most dialytic procedures because of their high plasma protein binding, especially to human serum albumin (HSA; MW 65.5 kDa). PBUTs circulate in the bloodstream in the form of bound and unbound, or free, fractions. The concentration of bound toxins is variable and depends on the binding affinity to plasma proteins, such as HSA.

The binding of uremic solutes to albumin involves both an equilibrium and a kinetic aspect in terms of reaction composition and rate equation [37,38]. The total concentration of the uremic solute can be calculated by adding the bound and free fractions, as described in Equation 4.

Where, $[US]_t$ is the total concentration of uremic solute, $[US]_b$ is the concentration of bound fraction, and $[US]_f$ is the concentration of free fraction of uremic solute. The free fraction of the solute (f) can be calculated by using the following ratio according to the Equation 5.

$$[US]_b = [US_t] - [US]_f \qquad \text{Equation 4}$$

$$f = \frac{[US]_f}{[US]_t}$$ Equation 5

The amount of free and bounded proportion depends on the affinity of toxins to the protein plasma. Mostly, there is a chemical equilibrium between the unbound and bound (including non-covalent binding). In most cases, protein binding is reversible, since both the toxin and the protein are involved in non-covalent bonds, such as electrostatic or hydrophobic interactions, dipole and van der Waals forces, and hydrogen bonds.

Generally, protein Human Serum Albumin has six binding sites of ligand association to albumin in normal ligand/albumin concentrations (Figure 9). Sudlow I and II are the most common binding sites regarding to protein binding of uremic toxins.

Indoxyl sulfate, p-cresyl sulfate, indole-3 acetic acid, and hippuric acid competitively share the same binding site, Sudlow's site II [39, 40] and 3-carboxy-4-methyl-5-propyl-2-furanpropanoic acid (CMPF) binds covalently to site I , the percentage of binding corresponding to each PBUTS is represented on Table 2 [5,40].

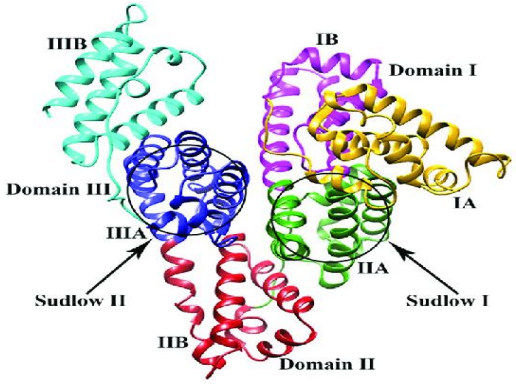

Figure 9-Binding sites of Human Serum Albumin [41]

Table 2- Percentage of binding (%) and high affinity site for each PBUTs adapted from [5,42].

PBUT´s	Protein Binding (%)	High affinity Binding site
P-cresyl sulfate	91-95	Site II
Indoxyl Sulfate	86-98	Site II
CMFT	>99	Site I
Indole 3-acetic acid	86-94	Site II

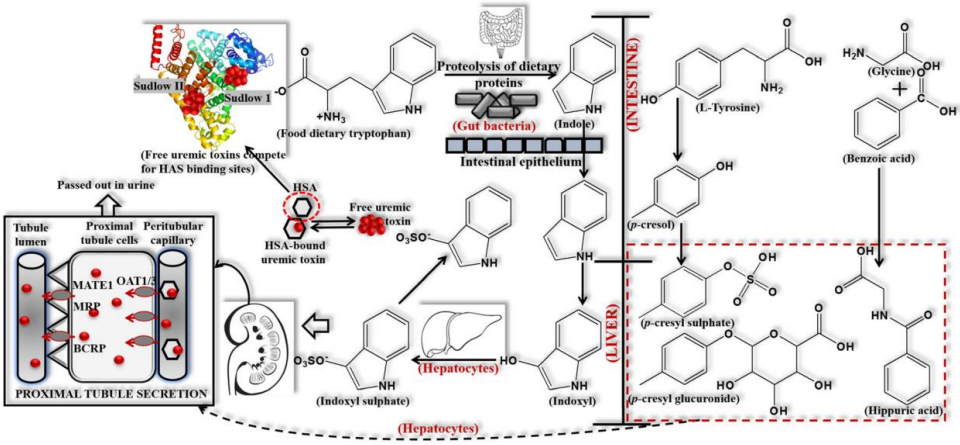

Figure 10- Pathway for production and clearance of protein-bound indoxyl sulfate (IS), p-cresyl sulphate (PCs), p-cresyl glucuronide (pCG) and hippuric acid (HA) toxins from the body. These PBUTs are excreted by active tubular secretion from the proximal tubular epithelial cells. As is clear, the problem is associated with the delimited parts of toxins that bind to the HSA and create a larger part that is difficult to remove. However, unbound parts can be excreted from the body [5].

2.3. Metal-organic frameworks (MOF) for the Removal of Protein-Bound Uremic Toxin from Human Serum Albumin

Metal-organic frameworks (MOFs) are porous crystalline polymeric structures formed by the coordination of metal ions, or clusters, with organic bridging ligands [43], to form 1D, 2D and 3D structures with regular and tunable pore structure, high thermal and mechanical stability.

Most MOFs are produced as fine powders, which are challenging to recycle in the industrial field. As a result of its properties, researchers began to focus on the synthesis and application of MOF membranes in the 2000s.

UiO66 is an archetypal metal-organic framework (MOF) with very high surface area as well as high thermal stability. UiO66 has garnered scientific appeal because to this, as well as its outstanding tunability and functionality, which is partly attributable to defect control of both missing cluster and missing-linker flaws. The combination of these properties results in a very versatile material that may be tailored to a wide range of applications.

UiO66 is a crystal containing metal nodes composed of a zirconium oxide complex bridged by terepthalic acid ligands. Terepthalic acid is 1, 4-BenzeneDicarboxylic acid (BDC). A representation of this structure is shown in figure below:

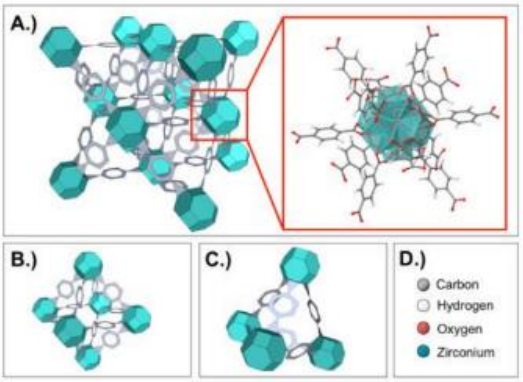

Figure 11- UiO66 structure, where: A- the face-centred cubic structure is composed of the metal node(blue) and ligand (grey) with atomic representation of the node and 12 connected BDC linkers. B-The node and ligand structure which compose the 12 A^0UiO66 cage. C-the node and ligand structure which composite the 7.6 A^0 cage. D-The color scheme for the atomic representation [44].

The apparent thermodynamic stability of UiO66 provided by the strong Zr-O bond has sparked interest; in fact, it has been discovered that the ligand's carbon-carbon bonds break down before the coordination link [45].

In addition, UiO66 has shown exceptional mechanical, thermal, acidic, aqueous, and water vapor stability. In terms of benchmark performance, the zirconium oxide node has demonstrated remarkable catalytic properties, and the overall stability and porosity of UiO66 has allowed it to function in aqueous applications such as pervaporation and dye adsorption.

Understanding the interactions between an adsorbent and the uremic toxins is critical for designing effective materials to remove these toxic compounds [45,46].

3.Framework and Thesis Objective

In the current study, the integration of UiO66 in pure CA and hybrid CA/SiO_2 membranes was investigated with the goal of enhancing the removal efficiency of p-cresyl sulphate (PCs). The UiO66 MOF was chosen because of its adsorption capabilities relative to PCs and other uremic toxins that had previously been studied under hemodialysis conditions and yielded favorable results.

The main objectives of this thesis are:

1. Synthesized CA, CA/SiO_2 membranes coupling wet phase inversion and sol-gel technique.
2. Synthesized MMMs: CA/UiO66 and CA/SiO_2/UiO66;
3. Pos-treat CA and CA/SiO_2 with solutions of: Glycerol (20%) and another solution of tritonX-100 and pure glycerol;
4. Study the membrane selective properties regarding: the hydraulic permeability of pure water, Molecular weight cut-off, apparent rejections to mono and divalent salts, and regarding uremic toxins;
5. Study the physical-chemical properties of the membranes synthesized by DSC and DRS measurements.

4. Materials and Experimental Methods

4.1 Materials

Membranes were synthesized with cellulose acetate (CA, $C_6H_7O_2(OH)_3$, 30 000 g/mol) with degree of acetylation of 39.8% from Sigma-Aldrich, formamide (CH_3NO, 45.02 g/mol, Panreac), pure acetone (C_3H_6O, 58.08 g/mol, ≥ 99.7%, José M. dos Santos, LDA), tetraethyl orthosilicate (TEOS) ,$Si(OC_2H_5)_4$ (208.33 g/mol, reagent grade 98%, Alfa Aesar), nitric acid (HNO_3, 63.01 g/mol,

65% v/v, Chem-Lab) and UiO66 ($Zr_6O4(OH)_4(C_6H_4C_2O_4)_6$, 1664.1 g/mol, synthesized in laboratory [47]).

Molecular weight cut-off (MWCO) was studied using polyethylene glycol (PEG) 3000 (2000 g/mol, Merck), PEG 6000 (6000 g/mol, Merck), PEG 10000 (10000 g/mol, Merck), PEG 20000 (20000 g/mol, Merck), PEG 35000 (35000 g/mol, Merck), PEG 40000 (40000 g/mol, Merck).

Permeation experiments were carried out with sodium chloride (NaCl, 58.44 g/mol, Panreac), urea ($CO(NH_2)_2$), 60.06 g/mol, Merck), potassium p-cresyl sulphate (PCs, $C_7H_7KO_4S$, 226.29 g/mol, synthesized by Professor João Paulo Telo [48]), bovine serum albumin (BSA, ~66500 g/mol, SigmaAldrich).

The reagents employed in the surface-active agent conditioning treatment were: Triton X-100 [$C_{14}H_{22}O(C_2H_4O)_{n,n=9}$] (Mw=647 g/mol) from VWR and Glycerol [$C_3H_8O_3$] (Mw=90.09 g/mol) supplied by PanReac.

4.2 Membrane Synthesis

Casting solutions of CA, CA/SiO_2, CA/UiO66, and CA/SiO_2/UiO66 membranes were synthesized by combining the processes of wet phase inversion, sol-gel, and direct MOF dispersing while maintaining a constant composition of SiO_2 and UiO66. The direct MOF blending approach was used to incorporate UiO66 in the membranes [49]. A polymer solution, or casting solution, containing cellulose acetate (CA, polymer), acetone (stronger/good solvent), and formamide (weaker solvent), is required for the phase inversion process.

Following the sol-gel process, the SiO_2 alkoxide sol-gel precursor, TEOS, was added and hydrolyzed by adding water and nitric acid to the casting [50]. The MOF UiO66 was directly added to the CA and CA/SiO_2 casting solutions.

When sol-gel hydrolysis and condensation occur under acid catalysis, the condensation rate at pH~3 (above the SiO_2 isoelectric point, IEP) is proportional to the concentration of

hydroxide groups, [OH], allowing the following chemical reactions [50,51] given sequentially by equations:

$$\equiv Si - OH + OH^- \xrightarrow{fast} \equiv Si - O^- + H_2O$$ Equation 6

$$\equiv Si - O^- + HO - Si \xrightarrow{slow} \equiv Si - O - Si \equiv + OH^-$$ Equation 7

Equation 8

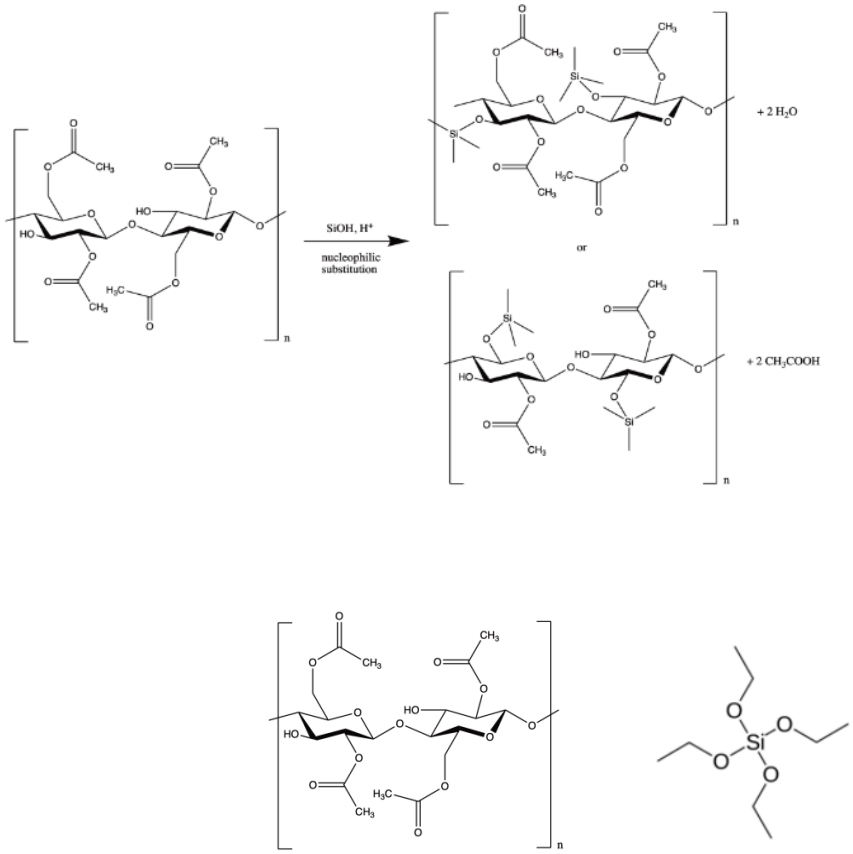

Figure 12- Structure of cellulose acetate and sol-gel silica precursor: TEOS, respectively.

Nucleophilic attack allows the creation of linear or highly branched polymeric species with a continuous three-dimensional fractal structure and nanopore sizes less than 2 nm at pH values less than 3 [50].

First, in alkoxide-based systems, Si-OR groups undergo hydrolysis to generate Si-OH groups (Equation 6), which are essential for condensation [50,51]. A homo-condensation reaction between silanol groups from the inorganic phase is possible (Equation 7). It is also envisaged that nucleophilic substitution will occur between Si-OH groups from the inorganic phase and C OH or COOH groups from the polymer (CA) phase, resulting in the formation of Si-O-C bonds [50] (Equation 8).

To make a thin polymeric film, the homogenized casting solution is applied to a suitable surface, such as a glass plate, while the solvent evaporation time is carefully controlled, and then the film precipitates in a deionized water coagulation bath. During the solvent evaporation time, acetone evaporates off the film surface that is in contact with the air. Because of evaporation, the amount of polymer at the surface in contact with the air increases during the solvent evaporation period, and the residual solvent in the film is insufficient to keep the polymer in solution. As a result, at that point, a skinned layer known as the active layer is produced. When the film formed on top of the glass plate is immersed in the coagulation bath, water and solvent diffusion occur in opposite directions, resulting in a porous structure. As a result, an asymmetric membrane is created, with a denser layer exposed to air on one surface and a porous sublayer in direct contact with the glass plate on the other.

The compositions of the casting solutions used to create CA, CA/SiO_2, CA_UiO66 and CA/SiO_2_UiO66 membranes are shown in Table 3. The contents of silica precursor (TEOS) and UiO66 were 5% and 1%, respectively, where the water used was deionized water.

Table 3-Casting solutions compositions (w/w %)

	CA	**CA/SiO_2**	**CA_UiO66**	**CA/SiO_2_UiO66**
CA	17	16.4	16.8	16.2
Formamide	22	21.3	21.8	21
Acetone	61	58.84	60.4	58.3
H2O	-	0.5	-	0.5
TEOS(SiO_2percursor)	-	3	-	3
UiO66	-	1	1	1

HNO_3	-	4 drops (pH~2)	-	4 drops (pH~2)

The casting solutions were prepared adding reagents by the following order: Cellulose acetate, formamide, acetone, TEOS, deionized water, and, finally, 4 drops of nitric acid are added to the mixture until get pH~2.

After that, the plastic flask is quickly covered and sealed with polypropylene tape (brown tape) and the flask was shaking vigorously until no polymer clumps are visible results in a preliminary homogeneity of the solution. After that, the solution is homogenized in a mechanical wrist action shaker for at least 24 hours at 600 rpm and room temperature. Finally, the solution is allowed to settle for 15 minutes to allow the air bubbles to coalesce before the membrane casting technique begins.

The addition of silica and the subsequent formation of complex C-O-Si three-dimensional networks would improve membrane selectivity and permeability, as well as antifouling capabilities and mechanical stability [52,53]. Acetone is used to dissolve cellulose acetate, resulting in a viscous casting solution. If the acetone/cellulose acetate ratio was too low, it would result in extremely viscous casting solutions that could not be used to produce uniform films. A high ratio, on the other hand, would result in thin sheets that, when submerged, would turn gelatinous [54].

Because formamide is not a true solvent for cellulose acetate, its primary role is that of a pore promoter [55,56]. In fact, formamide can be classified as a swelling agent [57], as it induces cellulose acetate to expand when exposed to it, resulting in an increase in the overall volume of the polymer-liquid system. It also enhances the capacity of acetate breakdown the polymer in solution [57]. As a result, after being exposed to air, acetone evaporates, causing the solution to approach the point of polymer precipitation.

The casting solutions conditions are represented in the following table:

Table 4-Casting solutions conditions

Temperature of solution (°C)	20-25
Room temperature (°C)	20-25
Air relative Humidity (%)	40-50
Solvent evaporation time (s)	30

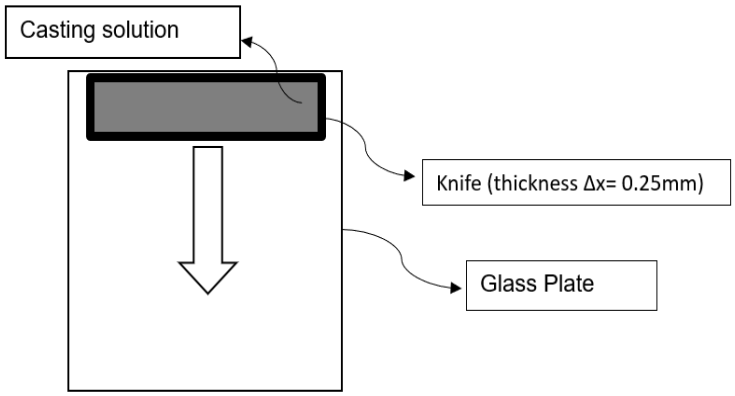

Figure 13- Casting solution techniques illustrated on a glass surface with a casting knife.

4.2.1. Membrane Post-treatment

The hybrid CA/SiO_2 membranes were conditioned in non-ionic surface-active agent solutions, triton X-100 and glycerol, following Vos et al. [58]. The following solutions were tested were three solutions tested: an aqueous solution of glycerol 20% (v/v), (G20), and an aqueous solution of triton X-100 4% (v/v) with glycerol 20% (v/v) (GT). In this post-treatment, each membrane was immersed for approximately 15 min.

Following that, the membranes are attached to a cord with metallic clamps and hung to dry inside a hotte for 1 hour under ambient circumstances. The membrane is then placed in a desiccator for 24 hours at room temperature to achieve complete evaporation of the reminiscent conditioning solution.

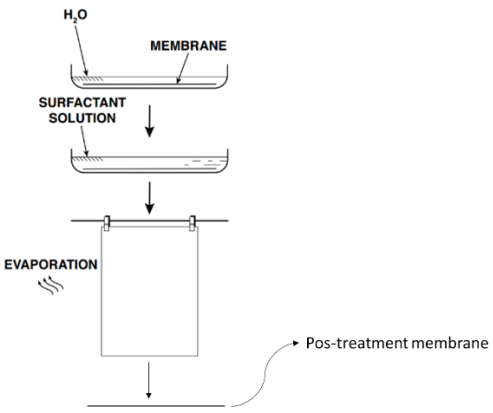

Figure 14- Schematic representation on the conditioning treatment using solutions of surface-active agents. Surfactant Solutions: a) Glycerol 20% (v/v) and b) Glycerol 20% +Triton X-100 4%(v/v)

4.3 Ultrafiltration installation

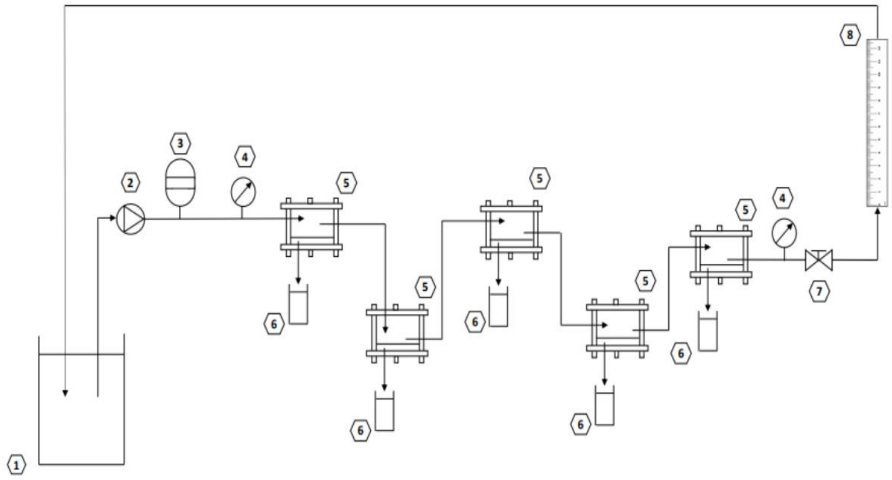

Figure 15-Crossflow Ultrafiltration Installation

This installation is composed by : **1**. Tank where is deposited feed solution (with thermometer to control the temperature); **2**. Cross-flow Pump **3**. Pressure damper to reduce pressure fluctuations downstream the pump; **4.** Manometers where pressure can be readable from 0 to 10 bar, and a precision of 0.25 bar in the 0-1 bar range and 0.2 bar in the 1-10 bar[20].; **5.** Five Permeation cells; **6.** Five Permeate tubes/Vials l ,where the permeate is collected by; **7**. Valve with function of control the pressure measured by the manometers in the inlet(before the

permeation) and outlet (after permeation); **8**. Rotameter scale from 0 to 100% uses to measure feed flow rate.

To calibrate the rotameter calibration its necessary to measure the flowrate (Q_F) by using a graduated cylinder and a chronometer, associating it to its % values on the scale. Moreover, its necessary to control the pressure and the feed flowrate by modifying the position of the back-pressure valve and the frequency of the pump. The calibration curve is shown in the **Appendix B.**

Furthermore, Throughout the experiment, the temperature of the feed fluid that circulates throughout the apparatus varies. Given this, the temperature throughout the experiment is the average of the initial and final temperatures.

The UF permeation cell is represent in:

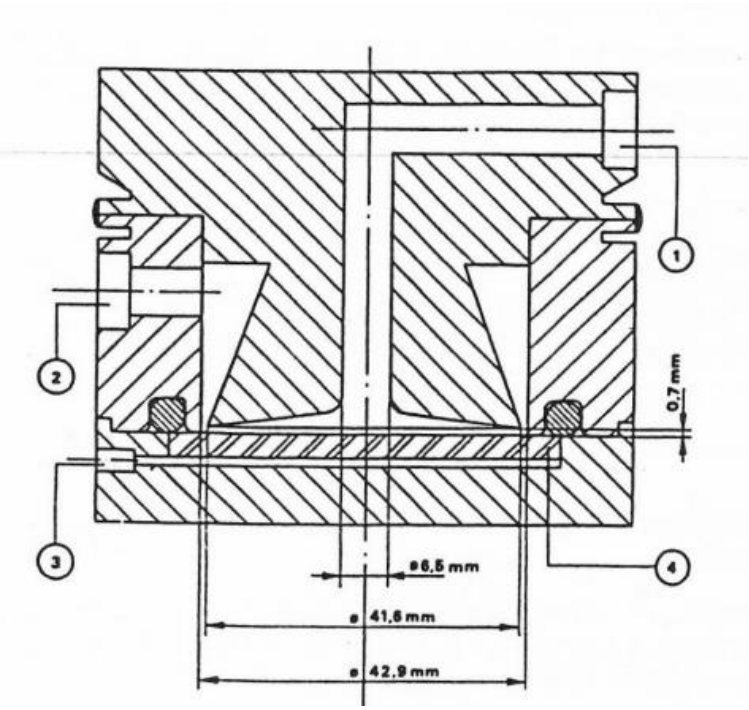

*Figure 16- Permeation cell where: **1.** Inlet feed solution; **2.** Outlet feed solution corresponds to retentate **3.** Permeate outlet; **4.** The membrane porous support [59,60].*

A Circular stainless steel porous plate that divides each cell into two sections mechanically supports the membrane. These two parts are held together by a two-metal frame plate mechanism that is bolted together to create proper sealing with the help of a Teflon ring infused

in the cell's upper half. The chamber of the pop of the cell's structure, which has a conical stage, considerably enhances the turbulence of the fluid flowing tangentially to the membrane when under pressure. This fluid dynamics provides to the reduction of concentration polarization in the fluid interphase near the membrane. The feed solution enters the cell axially to the membrane and exists radially throughout its perimeter as retentate. The feed solution enters the cell axially to the membrane and exists radially throughout its perimeter as retentate. Each of five cells has a permeation area of 13.4×10^{-4} m^2. The penetrated volume measured in short time intervals is substantially smaller than the 5 L flowing in the feed solution due to the limited membrane surface area. Because of the small membrane surface, the volume of the permeated are measured in short times in relation to the volume circulating in feed solution (V = 5 L).

Moreover, in each cell were introduced the following membranes respectively: CA, CA_UiO66, CA/SiO_2_UiO66, CA/SiO_2, CA/SiO_2_G20, these different membranes were tested with the same solution of feed, under the assumption of total recirculation mode is valid. Thus, the maximum number of permeation cells is limited by the feed volume to permeated volume ratio, in such a way that it does not produce substantial oscillations in feed solution concentration.

4.4 Ultrafiltration operation process and data acquisition

Because of the compression to which membranes are subjected during operation, hysteresis produces large permeability losses [61]. Thus, to minimize these losses, membranes were compressed to a pressure that is 20% higher than the maximum working pressure on the permeation experiments, in this case: 3.2 bar. To the compaction deionized water circulating through the installation at feed of maximum feed flux (Q_F = 3.27 L/min).

This UF experiment has four 4 different steps: installing start-up, stabilization of operating conditions, sample collecting period, and system turn off.

In the first step, before initializing the system, the valve was tested to see if it was completely open to avoid accumulating in the circuit. First step is the installing start up: before initializing the system, the valve was checked if it was completed open, to avoid the accumulation

in circuit. The pump is then turned on using a device (MOVITRAC LT) linked to it, and the pump frequency is gradually increased to achieve the necessary feed flowrate.

Second stage is the stabilization of operating conditions where operational circumstances must be stabilized. Depending on whether it is pure water or an aqueous solution, the system stabilized between 10 to 30 minutes. For aqueous solutions, the permeate samples are collected in a parafilm-sealed vial and recirculated to the feed tank during this time interval, which is set in total recirculation mode, so that the operating pressure, feed flowrate, and solution concentration in the feed and permeate can be stabilized.

Then, by the sample collecting step, the permeate samples are collected in vials with previously measured masses and deposited at the exit of the permeate channel, which is covered with parafilm. The time for each vial begins when the first drop of permeate falls, t_i, and ends when the last drop of permeate falls, t_f, once there is a quantifiable volume in the vial. The time interval, Δt t, during which permeation occurred is given by the difference between tf and ti. Finally, the mass, mf, of each vial is measured. The difference between initial mass(mi) and final mass(mf) allows to determine mass of each permeate sample, permeate mass (m_p).

Knowing the membrane surface area, Area of membrane it's possible to obtain permeate flux by Equation 9:

$$J_p = \frac{m_p}{t \times A_m} \qquad \text{Equation 9}$$

Finally, the system was turned off. To avoid damage to the membrane structure, the back-pressure valve is progressively opened after the permeation experiment to cause depressurization until the applied transmembrane pressure (ΔP_t) is null. Following that, the pump frequency is reduced to reduce the flowrate until it hits zero. After completing these steps, the pump can be turned off and unplugged.

Membrane washing was performed after each penetration experiment. This washing carried out in pure water at room temperature until the feed and permeate conductivities, as well as the permeate flowrate and, as a result, the hydraulic permeabilities, were identical to the starting values obtained for membrane characterization.

The washing procedure was carried out at the highest feed velocity, u_{max}, and at the lowest ΔP_t, which was close to zero. Hydraulic flushing removes surface deposits by creating a turbulent crossflow over the membrane surface towards the retentate side.

4.5 Membrane selective permeation properties

In the laboratory crossflow UF installation, the hybrid membranes were characterized in terms of hydraulic permeability, Molecular Weight Cut-Off (MWCO), apparent rejection coefficients to salts and to Uremic toxins: Urea, P_cresyl sulfate (PCs) and P_cresyl sulfate (PCs) with Bovine Serum Albumin (BSA).

The membranes referred in Table 3 were installed in the UF set-up represented in Figure 15.

4.5.1 Hydraulic permeability (L_p)

Hydraulic permeability (L_P) corresponds to the slope of the linear variation of the pure water permeate flux (J_w) as function of the transmembrane pressure (ΔP_t). All measures of the pure water permeate fluxes were taken at feed flow rate of 2.5 L/min, and transmembrane pressures ranging from 0.5 to 3 bar.

All data on mass permeate fluxes were corrected to 25 °C (Appendix A).

Transmembrane pressure (ΔP_t) notes the amount of force necessary to push water through a membrane. Concentration polarization and membrane fouling can occur in crossflow filtration, both of which reduce filtration efficiency [62]. Concentration polarization and hence fouling may be reduced when operating at an optimal specified range of ΔP_t and appropriate feed flow parameters [62]. ΔP_t is determined, as can be seen from Equation 10, as the difference from

the feed pressure, and the permeate pressure P_p. The feed pressure is an average between P_1 and P_2 representing inlet and outlet feed stream pressures, respectively.

$$\Delta P_t = \frac{(P_1 + P_2)}{2} - P_p \qquad \text{Equation 10}$$

4.5.2. Molecular Weight Cut off (MWCO)

The MWCO describes an ultrafiltration membrane's rejection capability. It is often expressed in Dalton (Da) and is the lowest molecular weight at which the rejection to neutral macromolecular solutes such as polyethylene glycol (PEG), dextran, and proteins of various molecular weights is at least ninety per cent (90%) [63,64].

Measuring the apparent rejection coefficients, f(%,) for PEGs with varying molecular weights enables the development of a MWCO retention curve.

A retention curve was constructed by determining the apparent rejection to each PEG as the MW increased. To compute the MWCO of each membrane, the MW of each PEG was: 2, 5, 10, 20, 35 and 40 kDa. The order used was required to achieve a 90% rejection with MW less than the highest established.

The apparent rejection coefficient(f) specified by Equation 11 .

$$\mathrm{f} = \frac{[[Concentration\ of\ the\ solute\ in\ \boldsymbol{feed}] - [Concentration\ of\ the\ soute\ in\ \boldsymbol{permeate}]]}{[Concentration\ of\ the\ solute\ in\ \boldsymbol{feed}]} \qquad \text{Equation 11}$$

Where: $[Concentration\ of\ the\ solute\ in\ \boldsymbol{feed}]$ is the average between feed initial and final concentration of feed.

Each permeation experiment was performed using aqueous solutions containing 600 ppm of each PEG in total recirculation mode (at the highest volumetric feed flowrate, which matched to the maximum velocity.

After 30 minutes of stabilization, each permeation experiment was performed using aqueous solutions containing 0.6 g/L of each PEG in total recirculation mode at the maximum volumetric feed flowrate and a transmembrane pressure of 1 bar. The concentration of solute in both feed and permeate samples were determined using a Total Organic Carbon Analyzer (TOC-VCPH/CPN, Shimadzu, Japan), through calibration curves for the used PEGs [65]. For all the membranes, the MWCO was determined based on the intersection of f_{app} curve as a function of molecular weight in kDa with the rejection line corresponding to f = 0.91.

4.5.3 Apparent rejection of salts

In this permeation experiments, one of a solution of a monovalent salt (NaCl) (600 ppm) and another experiment with solution of a divalent salt (Na_2SO_4) of 600 ppm was prepared. The permeate and feed samples were taken so that conductivity measurements could be made immediately corrected to 25 °C. The apparent rejection of the salts was determined by the Equation 11 and using previously a calibration curve [65].

The permeation experiments of this salt were carried out with total recirculation, and with maximum volumetric feed flowrate (3.37 L/min) at transmembrane pressure of 0.5 bar.

4.5.4. Apparent rejection of uremic toxins

The uremic toxins solutions were prepared due to reported concentrations: Urea: 0.4 g/L and 4.6 g/L corresponding to normal concentration and uremic concentration (CKD patient) respectively [66], 0.1 g/L of P_Cresyl sulfate [67] and 0.1 g/L PCs and 0.5 of BSA and 0.1 of BSA with 0.5 g/L of PCs.

In this permeation experiment the apparent rejection was determined by the same equation (Equation 11), but using two different methods .For the Urea permeations, the

measures of the concentrations of permeate and feed was measured in Total Organic Carbon equipment (TOC), described in and for PCs permeation, the measurements was on US-Vis spectrophotometer (US-1700 UV-1700 PharmaSpec, Shimadzu, Japan)with maximum absorbance wavelength of 265 nm using the calibration curve of PCs described in Appendix C.

The procedure of these all-permeation experiments is also in total recirculation and maximum Q_F = 3.27 L/min, with transmembrane pressure of 0.5, 1, 2 and 3 bar.

4.5.4.1 Apparent rejection of Uremic toxin bound to Bovine Serum Albumin (BSA)

In other hand, permeation of a uremic toxin, potassium p-cresyl sulphate, was tested with Bovine Serum Albumin (BSA). One scenario with excess of P_cresyl (0.5 g/L of P_cresyl and 0.1 g/L of BSA) and another with excess of Bovine Serum Albumin (0.5 g/L of BSA and 0.1 g/L of PCs).The first with molar fractions : PCs of 98.33%, BSA 1.67% and the last with: 99.93% of PCs and 0.07 % of BSA. In this permeation the apparent rejection refers to PCs

The feed solutions were previously heated to 37 °C (Temperature of human body) through to thermostatic bath. Thus ate the permeation experiments were carried at this temperature to allow the connection between the uremic toxin and BSA.

The measurements of the concentrations (of P_cresyl) was also done on US-Vis spectrophotometer (US-1700 UV-1700 PharmaSpec, Shimadzu, Japan) with maximum absorbance wavelength of 265 nm using the calibration curve described in Appendix D.

4.6. Analytic Methods

4.6.1 Dielectric relaxation spectroscopy (DRS)

Dielectric relaxation spectroscopy is a technique that operates in a frequency range of 10^{-2} to 10^{9} Hz, and it is commonly used in the study of molecular motions in amorphous materials. The

large frequency range allows probing movements very localized in the molecule, such as those corresponding to functional groups, and movements which involve several molecules or unities as it is the case of polymers. It is also indicated to charge transport properties.

When an oscillating electric field is applied to a dielectric material, the molecular charges shift from their equilibrium positions, resulting in polarization, which is a forced orientation of the charges in response to an applied electric field. The presence of permanent dipoles is required for obtaining a dielectric response. Thus, if the molecule is not dipole, it is not observing any response through this method. One of advantages of this spectroscopy is that the range of frequency is larger than another spectroscopy as we can see in figure below:

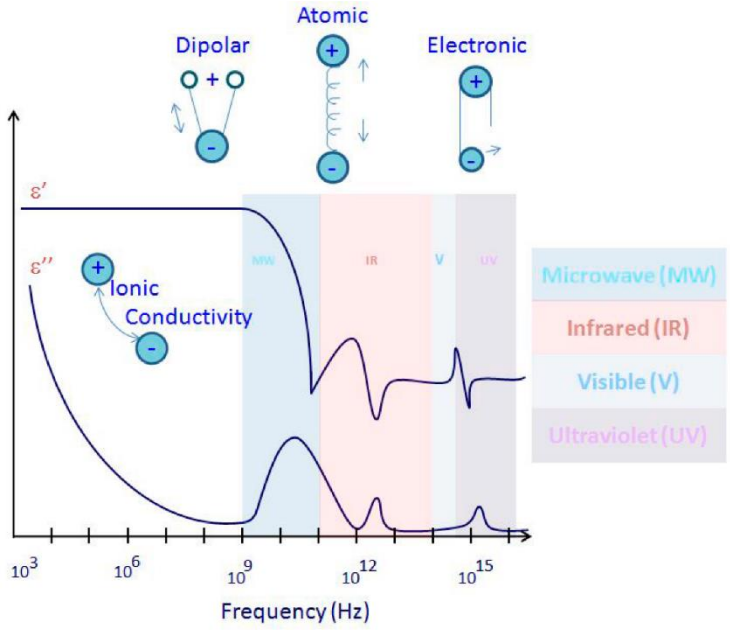

Figure 17- Polarization mechanisms versus the frequency range [68].

As it can see there are three polarization mechanisms [69] (Figure 17):

1. Electronic or induced polarization, which responds to field changes at all frequencies used instantaneously. In this type of polarization are involved resonance effects.
2. Dipole or orientational, that describes the movements of the dipoles which, depending on the frequency at the dielectric is subjected, will be able to follow all the displacements

associated with field polarizations. The response to the electric field is not immediate due to the resistance imposed to the dipole moment and to an irreversible loss of the free energy in the form of heat.

3. Interfacial polarization that occurs when charges are blocked at the interface between different dielectric constants, and the interface can be located within the dielectric. If it occurs in the contact region between the material and the electrode itself, this is called electrode polarization.

The complex dielectric constant (ε*) is given by relation between the electric field ($\vec{E}$) (stimulus) and polarization (P) (response) ($\vec{E} = \varepsilon^*.P$) This results in several processes, including fluctuations of molecular dipoles, the spread of moving charges, or the separation of interface charges that lead to more polarization, and is expressed as follows [69]:

$$\varepsilon^*(\omega) = \varepsilon'(\omega) - i\varepsilon''(\omega) \qquad \text{Equation 12}$$

The complex permittivity is used to considering the delay between the stimulus and the answer of the material.

The real part (ε ') of the dielectric constant, called permittivity, is related to the energy stored by the material and the imaginary part (ε") refers to the energy dissipated. The angular frequency, ω, is given by $\omega = 2\pi f$ that corresponds to the frequency of the oscillating electric field applied.

Each relaxation has an associated time that depends on the mobility of the molecules involved (dipoles) that constitute a material. The relaxation time (τ) corresponds to the time during the polarization created in the material by the external electric field decays a factor of 1/e, where e is the Neper number, after the field is removed. Thus, the relaxation time quantifies the process during which the distribution of the previously oriented dipoles returns to equilibrium, being randomly arranged [70].

While the frequency of the alternating electric field is applied is sufficiently slow, dipoles can follow the variations that they are subjected to. As the applied frequency increases, the energy, quantified by ε', begins to decrease due to the delay between the alignment of the dipole and the electric field. On the other hand, the dissipated energy of the system follows an opposite profile, increasing the imaginary part of the permittivity, ε". If the frequency of the field is above the maximum of the relaxation frequency, both components cease to exist, since the electric field is too fast to influence the dipoles oscillation and the orientational polarization disappears completely [70].

To extract the characteristic relaxation time of each relaxation, the Havriliak-Negami (HN) model function (Havriliak and Negami 1966)[71,72] or a sum of HN functions when multiple relaxations appeared) was used to analyze dielectric relaxation data:

$$\varepsilon^*(\omega) = \varepsilon_\infty + \sum_j \frac{\Delta\varepsilon_j}{[1 + (iw\tau_j)^{\alpha_{HNj}}]^{\beta_{HNj}}} \qquad \text{Equation 13}$$

$\Delta\varepsilon_j$ is the difference between the real permittivity values at the low and high frequency limits, τ_{HN} is Havriliak–Negami characteristic relaxation time of the dipolar relaxation process and α_{HNj} and β_{HNj} are shape parameters. The relaxation time $\tau_{max} = 1/(2\pi f_{max})$, where f_{max} is the frequency at the peak maximum appearing on the imaginary component (ε´´), of the complex permittivity.

The temperature dependence of the relaxation time for each peak observed in ε" vs. T represents the dynamic fingerprint of the compound. The molecular mobility originated by localized dipolar reorientations usually exhibits an Arrhenius temperature dependence:

$$\tau_{max} = \tau_0 \exp\left(\frac{E_a}{RT}\right) \qquad \text{Equation 14}$$

The dielectric analysis was done using M^* (dielectric modulus) instead of permittivity (ε^*). Its relation to given as: $M^* = \frac{1}{\varepsilon^*}$

4.6.1.1 Profile Temperature procedure

Dielectric measurements were carried out using the ALPHA-N impedance analyzer from Novocontrol Technologies GmbH, covering a frequency range from 0.1 Hz to 1 MHz. Each membrane sample were cut into disks with thickness ~ 0.045 mm, and was placed between two gold-plated electrodes of a parallel plate capacitor, BDS 1200. The sample cell was mounted on a BDS 1100 cryostat and exposed to a heated gas stream being evaporated from a liquid nitrogen dewar. The temperature was controlled by Quatro Cryosystem and performed within 0.5 K. The measurements start with a cooling ramp at 5 °C/min, from 20 °C to -120 °C, with data continuously taken at five selected frequencies (10^2, 10^3, 10^4, 10^5 and 10^6 Hz). After that, in steps of 5 °C, measurements were carried from -120 °C to 100 °C and -120 °C to 200 °C. Figure 18 represents in an schematic way the experimental procedure followed in dielectric measurements.

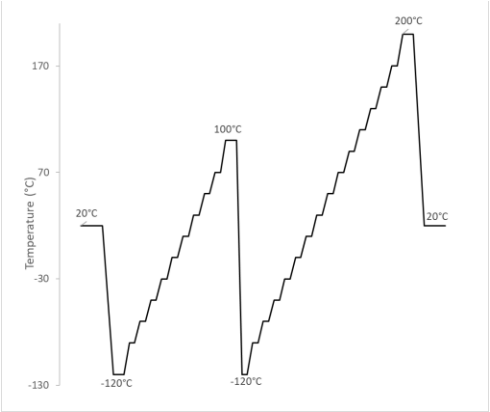

Figure 18- Temperature profile procedure during DRS experiment.

4.6.2 Differential Scanning Calorimetry (DSC)

Differential Scanning Calorimetry (DSC) is a type of thermal analysis that includes techniques for determining physical system parameters as a function of temperature. This analysis enables the characterization of physical phase transformations of systems.

A differential calorimeter uses a linear temperature ramp to measure the heat of a sample relative to a reference, and both the reference and the sample are at the same temperature throughout the experience.

It is this amount of heat required for transitions that is measured by DSC, permitting detect phase transformations as crystallization, melting and glass transition. Results are represented in a thermogram.

This type of thermal analysis that includes techniques for determining physical system parameters as a function of temperature. This analysis enables the characterization of physical phase transformations of systems [73]. And an amount of heat required for transitions that is measured by DSC, permitting detect phase transformations as crystallization, melting and glass transition. Results are represented in a thermogram where each peak corresponds to a process.

In DSC we can observed: A glass transition (T_g), a recrystallisation exotherm and a melting endotherm.

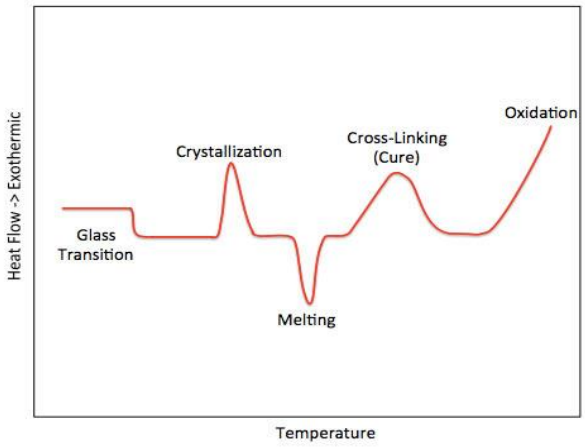

Figure 19-Thermal technique in differential scanning calorimetry [74].

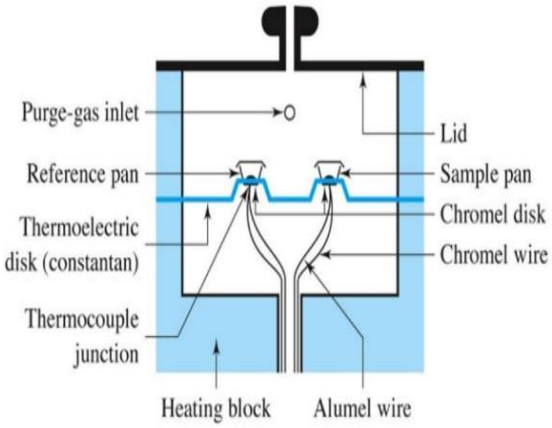

Figure 20- Heating flux [75]

One of the limitations of DSC measures, is that it only measures the sum or the heat flowrate from overlapping process. This makes quantitative analysis of the individual processes impossible and, it cannot optimize both sensitivity and resolution in a single experiment.

Regarding the limitations of DSC measurements mention above, another technique, was used in this work, Modulated Differential Scanning Calorimetry (MDSC).

Modulated Differential Scanning Calorimetry (MDSC) is another recent technique from DSC modification that adds a new dimension to the conventional approach. MDSC was developed that combines periodic temperature control performed by AC calorimetry and constant temperature control of the rate performed by standard DSC measurement [76,77] (Figure 21). MDSC heats samples by a temperature program that adds sinusoidal temperature control to linearly heating at constant rate. MDSC heats samples using a temperature program that incorporates sinusoidal temperature control in addition to linearly heating at a constant pace. By repeatedly heating and cooling the temperature in a short time, the sample temperature is elevated at a steady rate on average (Figure 15) [76]. In addition to information gained from standard DSC measurements, this method can simultaneously obtain heat capacity component (reversing heat flow) data that corresponds to the specific heat capacity while heating a sample at a steady pace by repeated sinusoidal temperature contrasts.

MDSC provides direct measurements of heat capacity, more accurate measurements of crystallinity, separation of complex transitions into more easily interpreted components, increased sensitive for detecting weak transitions and melts, increased resolution without loss of sensitivity.

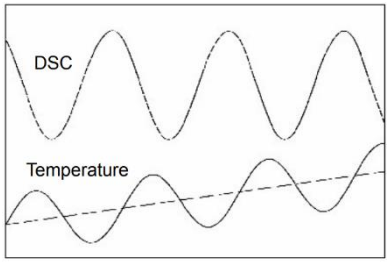

Figure 21- Temperature curve and DSC signal for TMDSC [76].

$$\frac{dH}{dt} = -C_p.\left(\frac{dT}{dt}\right) + f(T,t) \qquad \text{Equation 15}$$

Where:

- dH/dt: is the total heat flow due to the underlying or linear heating rate;
- Cp: Heat capacity component of the Total heat flow and is calculated from just the heat flow responds to the modulated heating rate;
- dT/dt: Measured heating rate, which has both a linear and sinusoidal (modulated) component;
- f(T/t): Kinect component of the heat flow and is calculated from difference between the Total signal and Heat capacity component;
- Cp.dT/dt: Reversing Heat flow component of the total heat flow.

According to Equation 15, the Total Heat Flow is made up of two distinct components: the heat capacity dependent component and the other phenomena (kinetic) dependent component.

The thermal features were examined using differential scanning calorimeter DSC Q2000 from TA Instruments Inc. (Tzero DSC technology) operating in the Heat Flow T4P option. Enthalpy (cell constant) and temperature calibration were based on the melting peak of indium standard (T_m = 156.60 °C). Membranes were cut into small pieces (approximately 5 mg) and introduced in an aluminum hermetic pan with a Tzero hermetic lid with a pinhole to facilitate the exit of water. Thermograms of all the membranes were obtained over a range of -80°C to 240°C at a heating rate of 5 °C/min under a nitrogen flow of 50 mL/min. Cooling ramps were conducted in the conventional mode while heating runs were done in the modulated one (modulated parameters: amplitude, A = ±0.663 °C, period, p = 50 s). In Figure 22 it can be seen a schematic representation of the Temperature-time experimental protocol followed in these measurements.

The data analysis was carried out using the software Universal Analysis 2000 from Thermal Analysis.

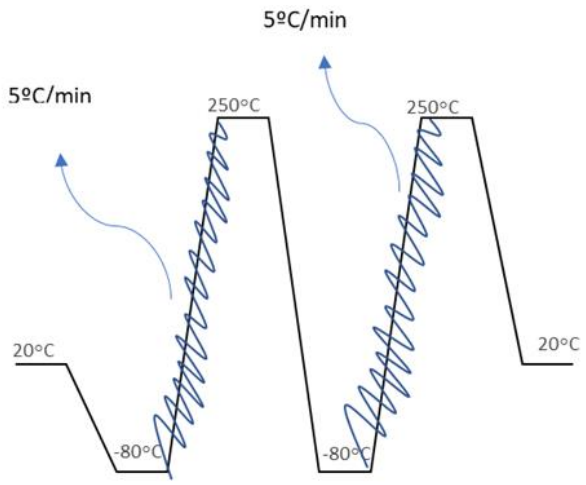

Figure 22-Profile temperature for TMDSC procedure.

4.6.3 Total Organic Carbon analysis TOC

Total organic carbon analysis (TOC) involves oxidizing all organic compounds into carbon dioxide (CO_2) by Nondispersive infrared (NDIR) sensor [78].

Total carbon (TC) refers to the sum of the contributions of organic and inorganic carbon. Therefore, the total organic carbon (TOC) is obtained by subtracting the inorganic carbon (IC) from the TC:

$$TOC = TC - TIC \qquad \text{Equation 16}$$

4.6.4 Conductivity

The electrolytic conductivity, σ, expressed in S/cm, is given by the equation represented below:

$$\sigma = G \times K \qquad \text{Equation 17}$$

where G is the conductance of a solution expressed in S units and K is multiplied by the cell constant (K) in cm^{-1}.

At a specific concentration and temperature, an electrolyte solution's conductance is a characteristic that is dependent on the cell being used to measure the solution [79], so the conductivity measurements depend on temperature. As Temperature has an impact on conductivity values, measurements of conductivity need to be corrected to a reference (T= 25°C) by the Equation 18 [80]:

$$\sigma_{T=25℃} = \frac{\sigma_T}{1 + (\frac{\sigma_{T=25℃}}{100})(T - 25)} \qquad \text{Equation 18}$$

where $\sigma_{T=25℃}$ is the conductivity measured at temperature of 25 °C.

A conductometer from Crison, model GLP 32, with a conductivity probe and a cell constant of $0.1 cm^{-1}$ was used to quantify the concentration of aqueous salt solutions (NaCl and Mg_2SO_4) with a typical temperature coefficient $\sigma_{T=25℃}$ = 2% [80].

4.6.5 US-Vis Spectroscopy

Because all organic compounds have valence electrons that can be stimulated to higher energy levels, they can all absorb electromagnetic radiation [81,82].

As a result of the high excitation energy associated with most single-bond electrons, absorption occurs in the region of ultraviolet with the lowest wavelengths (< 185nm).

However, most organic compound applications for absorption spectroscopy are based on transitions whose excited state energies from n or π electrons to the π^*excited state sends the absorption bands into the UV-visible (Vis) region (200 to 700 nm). An unsaturated functional group must be present for of these transitions($n \rightarrow \pi^*$and $\pi \rightarrow \pi^*$)to provide π orbitals [81,83]. Such functional groups enable the absorption of UV-Vis radiation by molecules.

Absorbance measurements were obtained using the spectrophotometer from Shimadzu, model UV-1700 PharmaSpec. For the absorbance measurements in the spectrophotometer, 2 quartz cells (1 cm path length) were used, one in which the sample is placed and another in which pure water used as blank.

5. Results and Discussion

5.1 Membrane characterization

5.1.1. Calorimetry results

All membranes were submitted to the same temperature-time profile consisting basically in two successive cooling/heating cycles. Results will be presented in first place the analysis for CA membrane and then, thermal events will be compared for the different samples prepared.

Upon cooling from 20 °C to -80 °C, the thermogram shows a large exothermal event whose onset is at -18 °C to related to the crystallization of bulk water (Figure 23(a)). At lower temperatures, close -40 °C, another small peak is observed (see arrow in the inset). On first heating, the melting of crystalline water starts around -18 °C (Figure 23(b)), and with minimum at -1.03 °C.

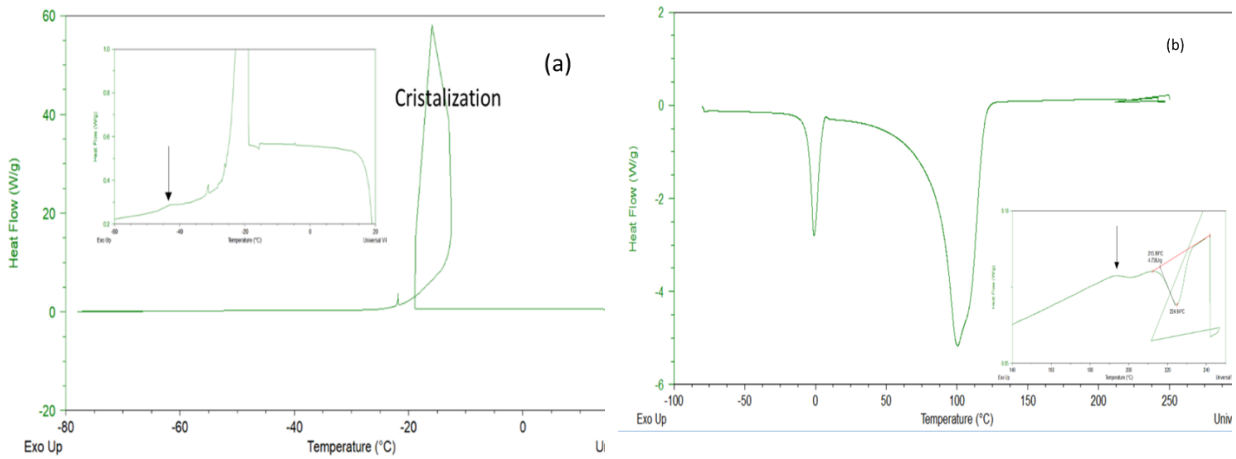

Figure 23- (a) Cooling thermogram for CA membrane (Inset graph is an ampliation of the small exothermal event around -18 °C (b) Heating thermogram obtained at 5 °C/min, A = ±0.663 °C and period p = 50 s (inset graph is an ampliation of the endothermal event around 250 °C).

Above room temperature, a large exothermal band is observed with minimum at 100.2 °C, corresponding to the water release form the membrane. Close to 200 °C, the heat flow shows a step indicating the glass transition of the dried membrane (arrow at Figure 23(b)). Immediately above the glass transition, an additional exothermal peak is detected (T_{min} = 224.9 °C) that can be associated to the melting of the crystalline fraction of the CA membrane. Also, the enthalpy calculated from the thermogram was ΔH_m = 8.4J/g (this value was corrected considering the water loss during the measurement). The crystallinity degree can be estimated by the ratio between the melting enthalpy of the material under study (ΔH_m) and the respective value for the totally crystalline material, ($\Delta H°_m$) by the equation below (Equation 19):

$$X_c(\%) = \frac{\Delta H_m}{\Delta H_m^\circ} \times 100 \qquad \text{Equation 19}$$

Where ΔH_m = 58.8 J/g as proposed by Cerqueira et al. [84] corresponding to 100% crystallinity for CA membrane, by this way the value of crystallinity degree is χ_c = 14.2 % for CA membrane (Table 5).

According to the literature [85], the crystallinity degree of CA membrane is X_c ~ 12%, that is similar to the estimated value of crystallinity degree in this work.

Table 5- Water loss ⊿m(%), Melting temperature, melting enthalpy (ΔH_m), melting enthalpy corrected by water loss, and crystallinity degree (%) values of CA, CA/SiO_2, CA_UiO66 and CA/SiO_2_UiO66 membranes.

	CA	CA/SiO_2	CA_UiO66	CA/SiO_2_UiO66
Initial sample mass (mg)	2.5	3.3	1.6	5.2
Final sample mass (mg)	1.6	0.8	0.54	0.8
Δm (%)	87.6	76.6	85.6	65.8
Melting Temperature (°C)	224.9	225.1	215.8	225.5
ΔH_m (melting enthalpy) (J/g)	5.3	3.8	1.6	0.9
ΔH_m corrected (J/g)	8.4	16.4	4.6	6.0
χ_c crystallinity degree (%)	14.2	27.8	7.8	10.2

The glass transition temperature (T_g) was determined during the 2nd Heating carried out under modulated conditions. In Figure 24, its possible to see how the glass transition temperature was estimated in the onset, midpoint and endset. The values are included in Table 6. The variation of the heat capacity (ΔC_p) as result of the increase of the degree of freedom at glass transition is 1.82 J/°Cg (corrected with the water loss). The values of T_g , variation of the heat capacity (ΔC_p), and the corrected variation of the heat capacity, $\Delta C_{p,corrected}$,were determined by the same procedure for the rest of membranes (Table 6). Comparing with litterature [86], the CA glass transition is ~ 196 °C , which is in the interval of the estmilated glass transition in this experiment (similar to the values estimated in this experiment (around 190 °C).

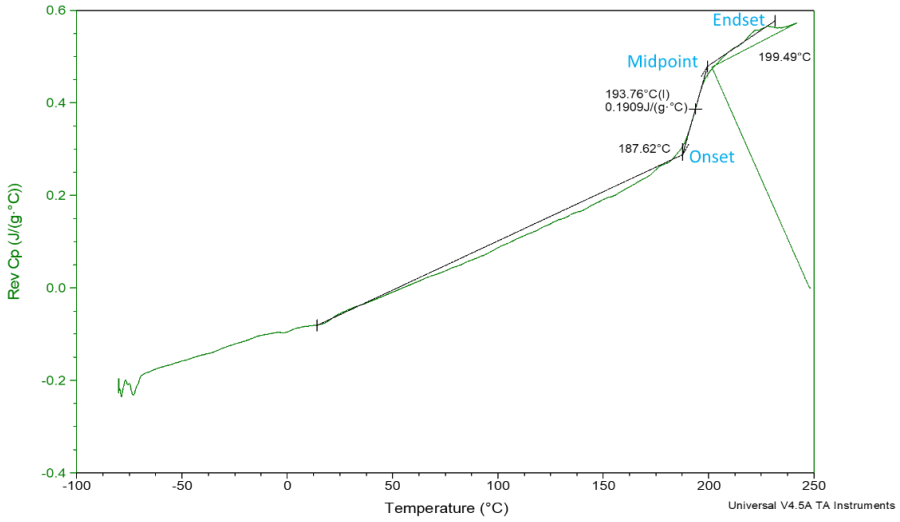

Figure 24- Reversing Cp obtained from MDSC experiment for CA membrane on heating at 5 °C/min.

Table 6- Representation of values of glass transition temperature determined in the onset, midpoint and endset, variation of the heat capacity (ΔC_p), and the corrected variation of the heat capacity ($\Delta C_{p,corrected}$) of CA,CA/SiO_2, CA_UiO66 and CA/SiO_2_UiO66 membranes.

		CA	**CA/SiO_2**	**CA_UiO66**	**CA/SiO_2_UiO66**
T_g	Onset (°C)	187.6	188.8	183.5	188.7
	Midpoint (°C)	193.8	192.4	191.4	192.7
	Endset (°C)	199.5	204.2	209.5	195.8
	ΔC_p (J/g◦C)	0.20	0.30	0.24	0.04
	$\Delta C_{p\ corrected}$ (J/g°C)	1.82	1.207	0.70	0.2

The same analysis was done for sample CA/SiO_2, CA_UiO66, and CA/SiO_2_UiO66 membranes. In Figure 25, there are represented the thermograms obtained on cooling (Figure (a)) and on heating (figure (b)). The water crystallization occurs in similar temperature for all the samples (Table 6), what is someway expected that it corresponds to bulk water. The CA and CA/SiO_2 membranes also presents a small peak at T = -41.98 °C (ΔH = 0.63 J/°C) as it was observed in CA (see arrows in figure Figure 25(a)). This exothermal peak would indicate that a fraction of

water recrystallizes at this temperature due to be located deeper inside the membrane like confined water reported in other materials [87].

Regarding the melting of water on heating (Figure 25(b)), the minimum temperature is similar for all the samples (~-1 °C).

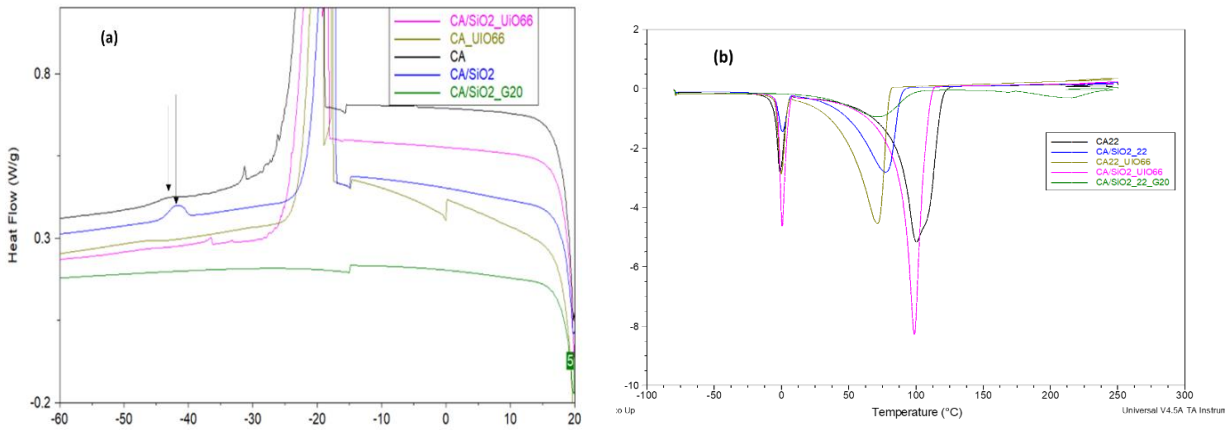

Figure 25- a) Cooling thermogram obtained at 5 °C/min for CA, CA/SiO_2, CA_UiO66 and CA/SiO_2_UiO66 membranes; Inset graph is an ampliation of the small exothermal event around -40 °C. (b) Heating thermogram obtained at 5 °C/min (A = ±0.663, p = 50 s) .

At higher temperatures, the water evaporation is clearly observed for all the samples, nevertheless the minimum occurs at different temperatures (Figure 25(b)). This may indicate strong/weak water-membrane interactions, then we can purpose an order: CA/SiO_2_G20, CA_UiO66, CA/SiO_2, CA/SiO_2_UiO66 and CA.

Above 150 °C, the glass transition signal and the melting of the membrane crystalline fraction are detected. As it can see in Table 5 , melting temperature does not change adding SiO_2 and/or MOF into CA membranes, therefore, the crystallinity degree changes. The crystallinity decreases by introducing MOF into CA and CA/SiO_2 membranes. Regarding the glass transitions (Table 6), it can be seen that the membranes have practically the same T_g and also the same heat

capacity variation, in CA/SiO_2_UiO66 membrane. The later lost a large amount of water, and the final mass of the membrane was very small, and it probably result in a poor DSC signal.

The main differences of the post-treated membranes refer to:

(i) There is no signal of bulk water recrystallization on cooling (and also the melting on heating);

(ii) Water evaporation is detected with $T_{minimum}$ at higher temperatures than in untreated membranes (Figure 26). This is expected since water in these membranes is not in bulk state and then it must be interacting with the polymeric structure;

(iii) At higher temperatures the glass transition step is not clear at the heat flow, and two successive peaks are very well defined (T_{min1} = 57 °C and T_{min2} = 158 °C for CA_GT membrane (for example);

(iv) The second peak can be assigned to melting since it occurs at a similar temperature of crystalline melting in untreated membranes (Table 7). However, the high values of enthalpy obtained means that it is not only the CA part of the membrane;

(v) The glass transition temperature (Table 8) taken on the second heating is nearly unchanged by the presence of glycerol, glycerol-triton.

Table 7- Mass loss ⊿m(%), Melting temperature, melting enthalpy (ΔH_m), melting enthalpy corrected by water loss, and crystallinity degree (%) values of post-treated membranes.

	CA_G20	CA/SiO_2_G20	CA_GT	CA/SiO_2_GT
Initial sample mass (mg)	2.5	3.8	1.9	2.7
Final sample mass (mg)	1.6	1.47	1.27	1.2
Δm (%)	37	63	36	56.3

Melting Temperature (°C)	213.7	213.5	208.2	209.1
Melting enthalpy, ΔH_m (J/g)	119.7	106.1	166.8	189
Melting enthalpy corrected, $\Delta H_{m,corrected}$ (J/g)	190.5	277.2	260.1	432.5

Table 8- Representation of values of glass transition: Onset, Midpoint and Endset, variation of the heat capacity (ΔC_p) ,and the corrected variation of the heat capacity ($\Delta C_{p,corrected}$) of Post-treated membranes.

		CA_G20	CA/SiO_2_G20	CA_GT	CA/SiO_2-GT
T_g	Onset (°C)	176.9	164.8	157.6	165.6
	Midset (°C)	191.4	190.9	175.5	195
	Endset (°C)	208.7	202.8	197.6	204.5
	ΔC_p (J/g°C)	0.43	0.27	0.4	0.41
	ΔC_p corrected (J/g°C)	0.69	0.71	0.62	0.93

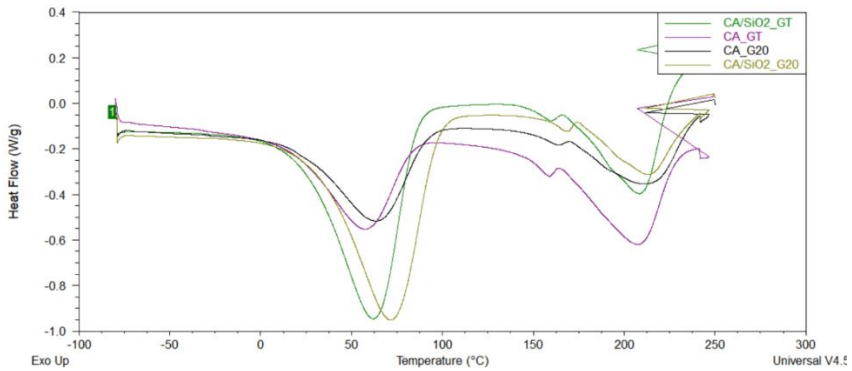

Figure 26- Heating thermogram obtained at 5 °C/min, A = ±0.663 and p = 50 s for post-treated membranes.

5.1.2. Dielectric Relaxation Spectroscopy results

First, as mentioned before, membranes were submitted to a cooling ramp from 20 °C to -80 °C (at 5 °C/min) and then, two successive heating's, the first one from -120 °C to 100 °C (serie 1) and the second one, from -100 °C to 200 °C (serie 2). While during cooling ramp only five frequencies were used to monitor the permittivity, on heatings, isothermal spectra with frequencies ranging from 0.1 Hz to 10^6 MHz, were collected every 5 degrees (note that every

isothermic spends approximately 10 minutes, then the equivalent heating rate is around 5 °C/min). In Figure 27- Imaginary part of (a) complex permittivity (ε´´) and (b) complex dielectric modulus (M´´) at f = 103 Hz for CA membrane: cooling ramp at 5 °C/min, black symbols, heating isothermal spectra (serie 1), orange symbols, and heating isothermal spectra (serie 2), blue symbols.

(a) it is represented the imaginary part (ε´´) of the complex permittivity as a function of temperature for the frequency of 10^3 Hz; in Figure 27- Imaginary part of (a) complex permittivity (ε´´) and (b) complex dielectric modulus (M´´) at f = 103 Hz for CA membrane: cooling ramp at 5 °C/min, black symbols, heating isothermal spectra (serie 1), orange symbols, and heating isothermal spectra (serie 2), blue symbols.

(b) it is represented the corresponding imaginary part of M* showing a similar profile than ε´´(T) .

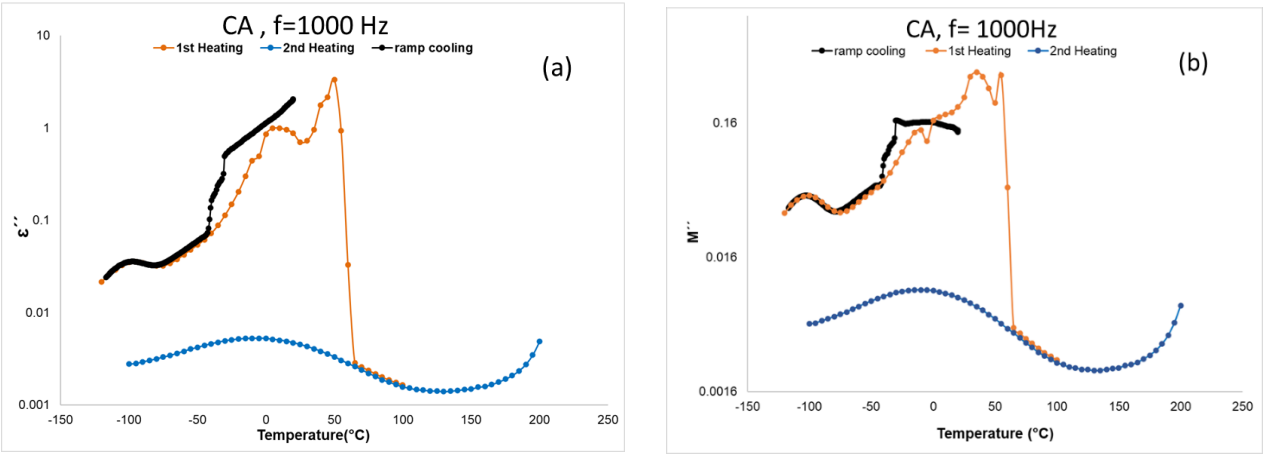

Figure 27- Imaginary part of (a) complex permittivity (ε´´) and (b) complex dielectric modulus (M´´) at f = 10^3 Hz for CA membrane: cooling ramp at 5 °C/min, black symbols, heating isothermal spectra (serie 1), orange symbols, and heating isothermal spectra (serie 2), blue symbols.

From DSC analysis, it was shown that bulk water recrystallizes on cooling ramp. This phenomenon is also observed in dielectric results by a decrease in ε´´ (or M´´) at -30 °C. With continuous cooling, the ε´´(T) trace allows distinguish at least one dipolar relaxation around -100 °C.

On the first heating (orange circles in Figure 27- Imaginary part of (a) complex permittivity (ε´´) and (b) complex dielectric modulus (M´´) at f = 103 Hz for CA membrane: cooling ramp at 5 °C/min, black symbols, heating isothermal spectra (serie 1), orange symbols, and heating isothermal spectra (serie 2), blue symbols.

) At higher temperatures close to 50 °C, during first series, a sharp decrease is observed. As it will be seen later by DSC, it corresponds to the water evaporation. In the second series (blue circles), a broad and low intense relaxation is observed who's maximum (at the frequency displayed) is close below 0 °C.

Figure 28 displays some representative M´´(f) spectra from -55 to 10 °C in which multiple relaxations can be directly seen. To extract dynamical information, each isothermal spectrum has been deconvoluted in the individual relaxations by using a sum of HN equations (imaginary component). Examples of this data treatment are included in Figure 29 for spectra collected at -100, -50 and 0 °C.

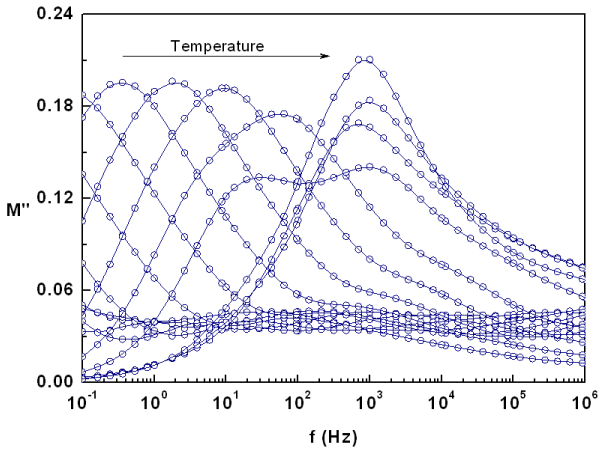

Figure 28- Frequency dependence of the imaginary part of the complex dielectric modulus from -55 °C to 5 °C in steps of 10 °C for CA membrane.

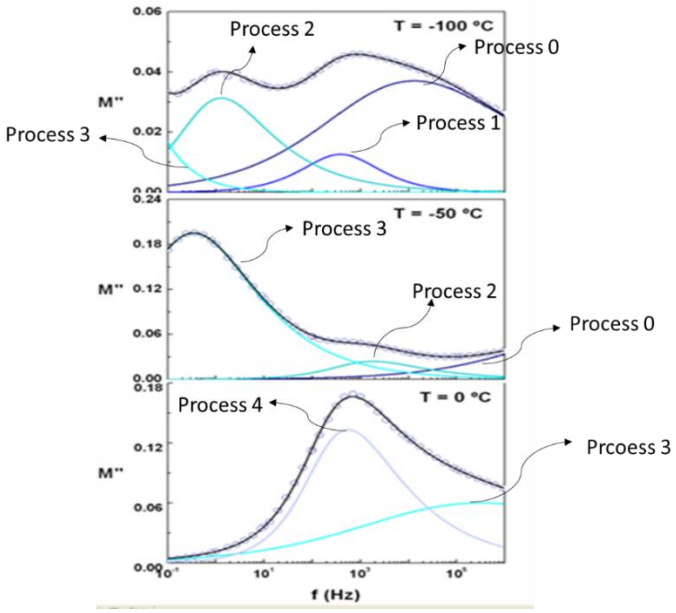

Figure 29- Isothermal data collected at -100, -50 and 0 °C (blue circles) and the corresponding processes for CA membrane. The individual HN fitting functions used are blue lines, and the overall fit is depicted as black line.

By this data treatment up to six relaxations were distinguished whose shift to higher frequencies as the temperature increases. In Table 9- Fitting parameters αHN, βHN and are summarized the α_{HN}, β_{HN} and ΔT fitting parameters used for all the relaxations. Additionality the principal parameter obtained was characteristic relaxation time, τ_{HN}, that was convert to the model-independent, τ by the next equation:

$$\tau_{max} = \tau_{HN}\left[sin\left(\frac{\alpha_{HN}\pi}{2+2\beta_{HN}}\right)\right]^{-\frac{1}{\alpha_{HN}}}\left[sin\left(\frac{\alpha_{HN}\beta_{HN}\pi}{2+2\beta_{HN}}\right)\right]^{-\frac{1}{\alpha_{HN}}} \qquad \text{Equation 20}$$

Table 9- Fitting parameters α_{HN}, β_{HN} and corresponding T range of CA membrane.

	Process 0	Process 1	Process 2	Process 3	Process 4	Process 5
α_{HN}	0.36	0.7	0.72	0.6	0.8	0.7
β_{HN}	0.6	1	0.55	0.5	1	0.5
T range (°C)	[-110,-60]	[-110,-70]	[-105,-15]	[-55,5]	[-20,55]	[50,55]

The relaxation times estimated by this way have been represented against the reciprocal of temperature in Figure 30. From the relaxation map some features can be underlined:

(i) All processes follow a linear temperature dependence that can be well described by an Arrhenius-type equation, whose activation energies and pre-exponential factor are included in **Erro! A origem da referência não foi encontrada.**.

(ii) As temperature increases, process 1 tend to merge with process 2 (see arrow in Figure 30);

(iii) Process 3 and 4 undergoes a change from a linear trend to another with a high slope at around T ~270 °C (~3.7 = 1000/T(K)).

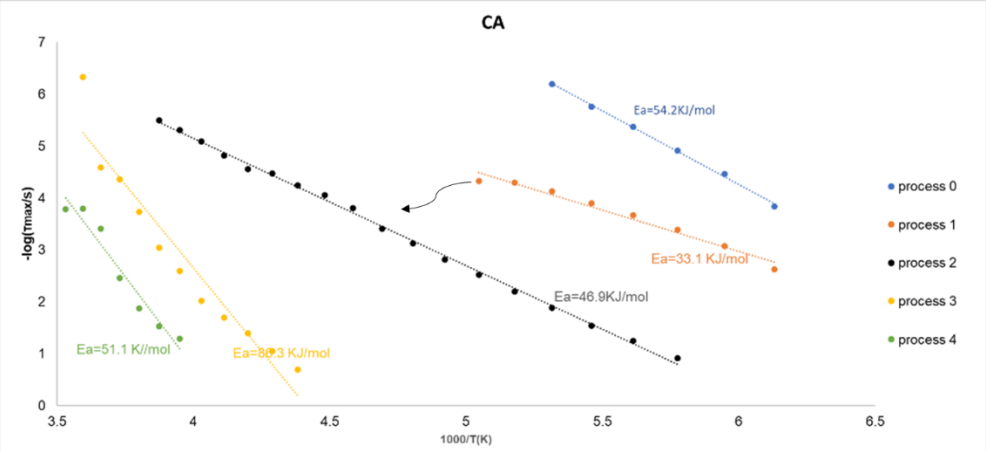

Figure 30- Temperature dependence of relaxation times, τ_{max}, for processes detected in CA membrane (serie 1). Lines correspond to the fitting with an Arrhenius-type equation, and activation energy (E_a) values in kJ/mol corresponding each CA membrane processes.

The linear trend is a common feature to all the processes, and as it was referred in the experimental section, it can be described by Arrhenius equations.

Table 10- Activation energy E_a (kJ/mol) and time at infinite temperatures (τ_0) values of CA membrane processes.

	Process 0	Process 1	Process 2	Process 3	Process 4	Process 5

E_a(kJ/mol)	54.2	33.1	46.9	86.3	51.1	57.5
τ_0 (s)	5.6E-22	4.9E-14	1.1E-15	4.4E-21	5.9E-15	1.23E-13

The literature values of the estimated Arrhenius Parameters: activation energy and pre-exponential factor for CA membrane [85] are for process I E_a = 44.3 kJ/mol and $\tau_0 = 3\times10^{-16}$ s, and process II: 64.3 and $\tau_0 = 3 \times 10^{-16}$ (Figure 31). Where can be comparing with CA membrane analyzed in this experiment. Therefore, the process I of the literature is similar to process 2 (Figure 30), and process II to process 3 (Figure 30).

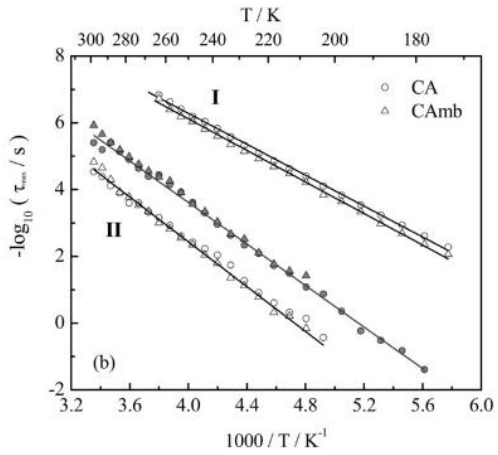

*Figure 31- Relaxation map for processes I and II detected in CA (2.73% w/w water) and CAmb (1.60% w/w water) open symbols. Full symbols stand for $\tau_{max}(T)$ of the remaining process in both samples after dehydration [**Erro! Marcador não definido.**].*

The presence of SiO_2 and/or MOF induces significant changes in dielectric modulus as shown in Figure 32. Al lowest temperatures, two very well-defined relaxations are visible in those membranes while only one was distinguished in CA. Another significant difference occurs at 0 °C, temperature at which the three "complex" membranes show a sharp decrease in M´´, while something similar was observed in CA only at higher temperatures (~50 °C). The origin of this change cannot be attributed to water evaporation but rather it may be related to melting. Above 0 °C, M´´ increases gradually for three samples up to a temperature 65, 80 and 95 °C for CA/SiO_2, CA_UiO66 and CA/SiO_2_UiO66 respectively, and then decreases.

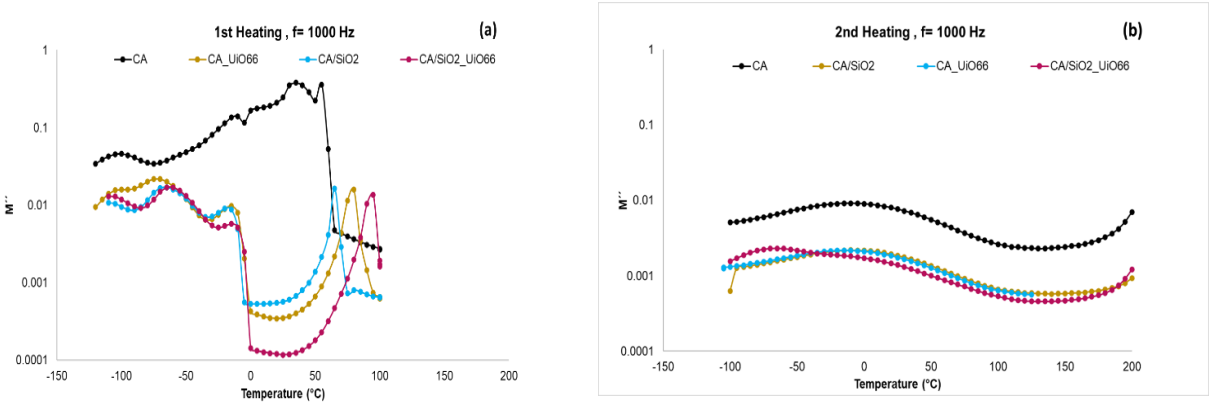

Figure 32- 1st Heating M´´ vs. Temperature (°C) at frequency of 10^3 Hz of CA, CA_UiO66, CA/SiO_2_22 and CA/SiO_2_UiO66 membranes. (b) 2nd Heating M´´ vs Temperature (°C) at frequency of 10^3 Hz of CA, CA_UiO66, CA/SiO_2 and CA/SiO_2_UiO66 membranes.

In the second heating (serie 2), M´´(T) is similar for CA, CA/SiO_2 and CA_UiO66 and CA/SiO_2_UiO66 for which only one very much extended relaxation is detected. In CA/SiO_2_UiO66 an additional relaxation is observed at lowest temperatures (maximum around -80 °C).

As mentioned before, the relaxation times extracted from HN fits are reported in Figure 33 (examples of fitted spectra can be found in supplementary material as well as fitting parameters, Appendix H). The main difference relatively to CA refers to the number of relaxation

deconvoluted during the fitting procedure of isothermal spectra, that was reduced from five in CA to three with CA and SiO_2 and/or MOF.

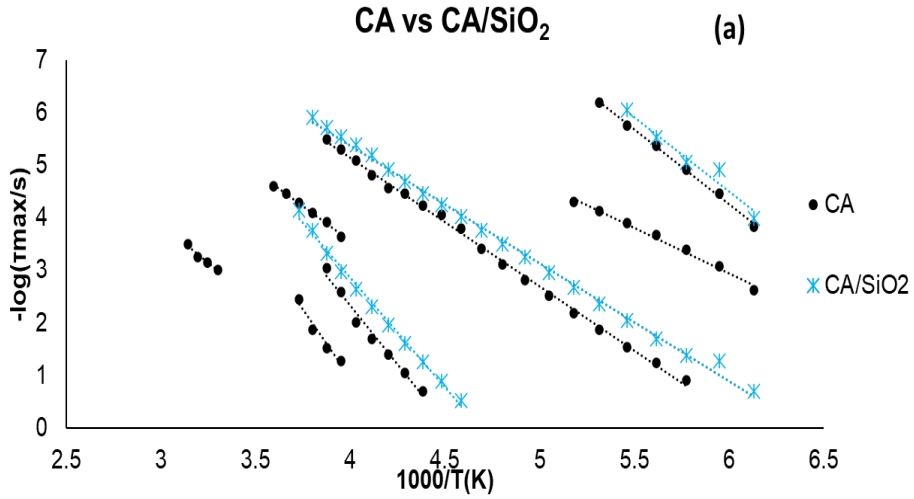

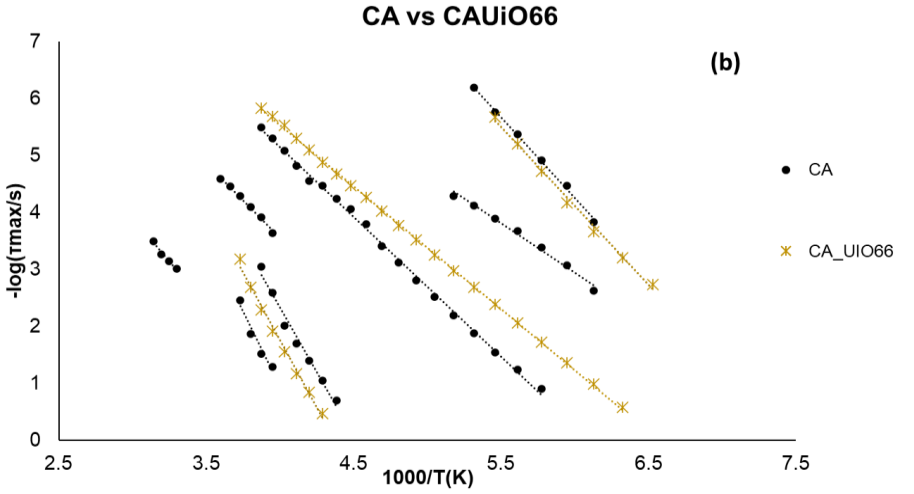

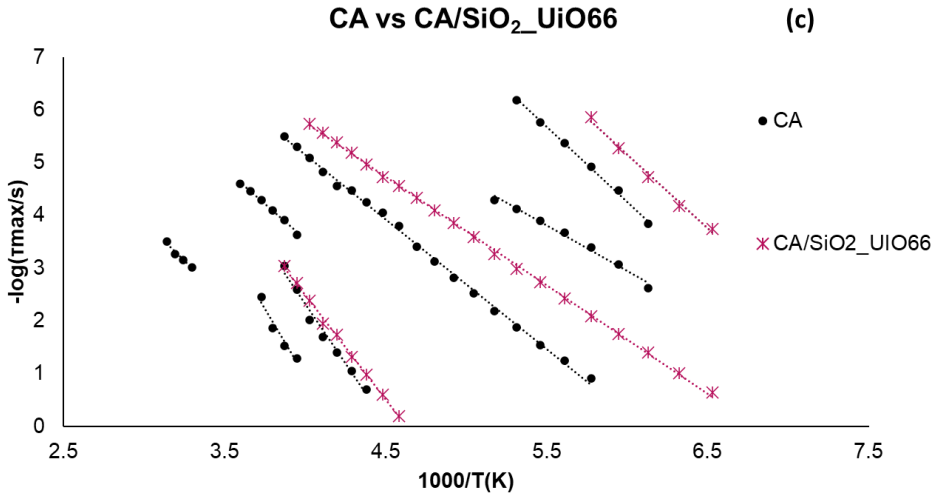

Figure 33- Relaxation map of CA membrane compared with the corresponding for: (a) CA/SiO_2, (b) CA_UiO66 and (c) CA/SiO_2_UiO66 membranes.

For each relaxation it was possible to calculate the Activation energy (E_a) in kJ/mol and the time at infinite temperatures (τ_0) (equation 10) which are represented in the following table:

Table 11- Activation Energy, E_a, in kJ/mol, and pre-exponential factor, τ_0, in sec values of CA/SiO_2, CA_UiO66 and CA/SiO_2_UiO66 membranes.

	CA/SiO_2			CA_UiO66			CA/SiO_2_UiO66		
	Process 0	Process 1	Process 2	Process 0	Process 1	Process 2	Process 0	Process 1	Process 2
E_a (KJ/mol)	54.1	42.9	77.3	53.1	39.1	84.0	53.9	39.4	75.2
τ_0	3.6E-22	4.6E-15	1.1E-19	1.8E-21	1.3E-14	5.2E-20	9.2E-23	1.0E-14	2.6E-19

As it can see in Table 11, the Activation energy values for each membrane process does not significantly change for CA/SiO_2, CA_UiO66 and CA/SiO_2_UiO66 membranes, neither τ_0.

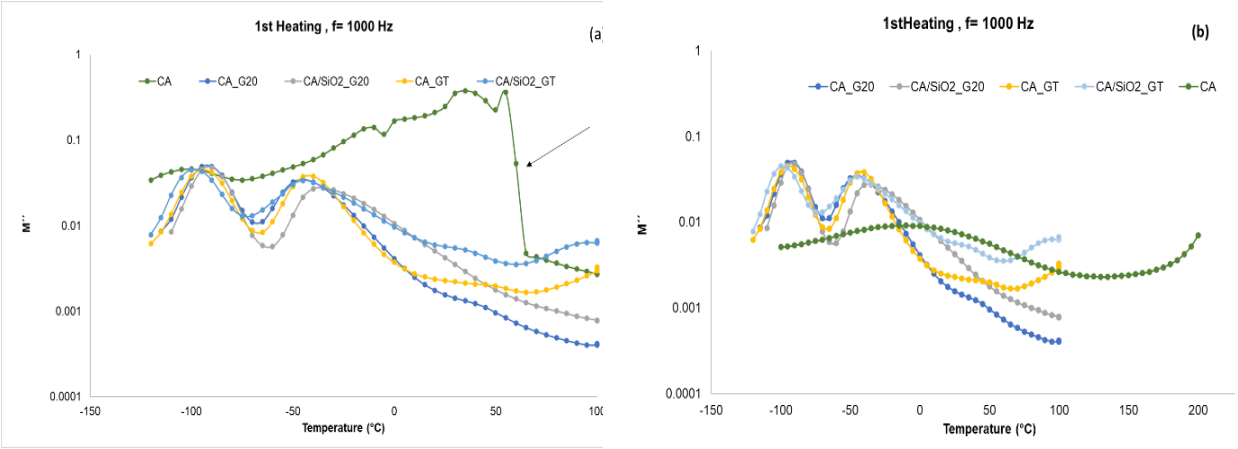

Figure 34- 1st (a)and 2nd Heating (b) M´´ vs Temperature (°C) at frequency of 10^3 Hz of CA, CA_G20, CA/SiO_2_G20, CA_GT and CA/SiO_2_GT membranes.

Concerning the post-treatment, the isochronal representation of M´´ shows the following differences:

(i) At lowest temeprtures a narrow relaxation is observed, very different to that found in CA, CA/SiO_2 and/orMOF membranes.

(ii) The sharp decrease (see in arrow Figure 34) in M´´ at ~50 °C in CA has not equivalent in the glycerol treated membrane;

(iii) The suddently decrease observed in untreated CA membrane at ~50°C associated to water removal (green symbols in Figure 34(a) is not onsereved in CA/SiO_2_G20.

(iv) In the second series, the broad relaxation visible in CA and CA/SiO_2 is not observed in glycerol treated membrane, which keeps the profile observed in the first serie.

In Figure 35, it is displayed the relaxation map of all the treated membranes. It is noticeable the non-Arrhenius temperature behavior of the more intense peak observed at lower temperatures. This tendency can be described by a VFTH function [88]:

$$\tau_{max} = \tau_{\infty} \exp^{\frac{B}{T-T0}} \qquad \text{Equation 21}$$

where B, τ_∞ and T_0 are fitting parameters. The obtained parameters for this sample were B = 2040.4 K, T_0 = 110 K and τ_∞ = 11.14 s (Figure 35). This is commonly used the fitting function to

extrapolate a glass transition temperature to τ_{max} = 100 s [89] that in this case was 5.7 K (-95 °C). This value matches well with the corresponding to bulk glycerol [90] and consequently, the relaxation detected in CA_GT can be assigned to "residual" glycerol incorporated in the membrane. This conclusion can be also applied to other membranes post-treated with glycerol solutions.

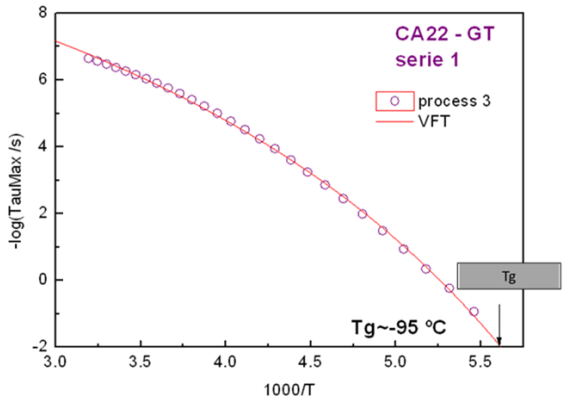

Figure 35- Relaxation map of CA_GT membrane for spectra collected in the first serie. Corresponding to the fitting with VFTH equation (curved).

Table 12- Activation Energy E_a (kJ/mol) and time at infinite temperatures (τ_0) values of CA/SiO_2, CA_UiO66 and CA/SiO_2_UiO66 membranes.

	CA_G20		CA/SiO_2_G20		CA_ GT			CA/SiO_2_GT	
	Process 0	Process 1	Process 0	Process 1	Pro-cess 1	Process 2	Process 3	Pro-cess 1	Process 2
E_a (kJ/mol)	93.1	101.7	27.7	91.9	90.5	122.9	64.8	76.1	113.4
τ_0 (s)	1.2E-31	2.5E-33	1.1E-14	5.4E-31	1.9E-31	1.7E-39	3.7E-15	7.1E-27	3.6E-36

Activation energy values obtained for relaxation fitted by Arrhenius equation (Equation 14) are significantly higher than those observed in untreated membranes. These results suggest that the molecular origin is mainly associated to glycerol (or glycerol-membrane) and not water (water-membrane) as in the untreated membranes.

5.2. Permeation characterization

5.2.1. Hydraulic permeability (L_p)

The hydraulic permeability (L_p) was determined for each membrane by representing graphically the pure water permeation fluxes, J_W (corrected at 25 °C), as function of transmembrane pressures, ΔP_t: 0.5, 1, 2 and 3 bar.

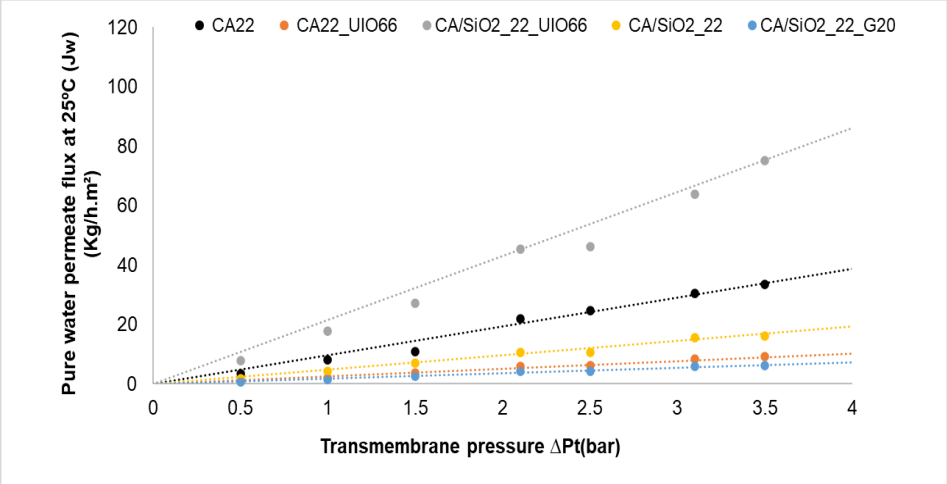

Figure 36- Pure water permeate mass flux at 25 °C, as a function of the applied transmembrane pressure from 0.5 to 4 bar and for each membrane. The permeate fluxes were measured at a volumetric feed flow rate of 2.5 L/min and with a membrane surface area of 13.2 ×10^{-4} m^2.

The slope of each linearization's represented in figure above (Figure 36) corresponds to hydraulic permeability of each membrane. In figure below are presented the hydraulic permeabilities (at 25 °C) that corresponds to each membrane:

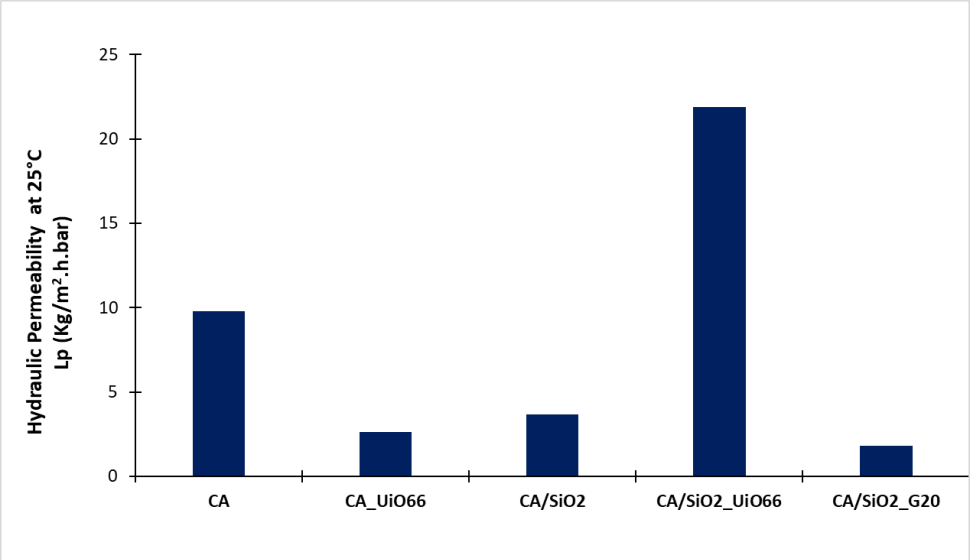

Figure 37-Hydraulic permeability at 25 °C, (L_P) in kg/ (h.m^2.bar) for all the membranes. The L_P 25 °C were obtained in the ΔP_t range from 0.5 to 4 bar, with a surface area, Am, of 13.2 × 10^{-4} m^2 at a volumetric feed flow rate, Q_F, of 2.37 L/min.

As it can be seen, by introducing MOF in CA membrane the permeability decrease, and with CA/SiO_2 membrane the opposite happens, CA/SiO_2 permeability is lower than the one of CA/SiO_2_UiO66, and the lowest permeability is CA/SiO_2_G20.

5.2.2. Molecular weight cut off (MWCO)

The Ultrafiltration is carried out for aqueous solutions of solute with increasing molecular weight: PEG 3, 6,10 , 20, 35 and 40 kDa. The apparent rejection coefficient to these solutes is plotted versus its molecular weight to yield the curves fitting these data and shown in Figure 38 to Figure 42.The intersection of these curves with the line of an apparent rejection coefficient of 91% gives the molecular weight that corresponds to the Molecular Weight Cut-Off.

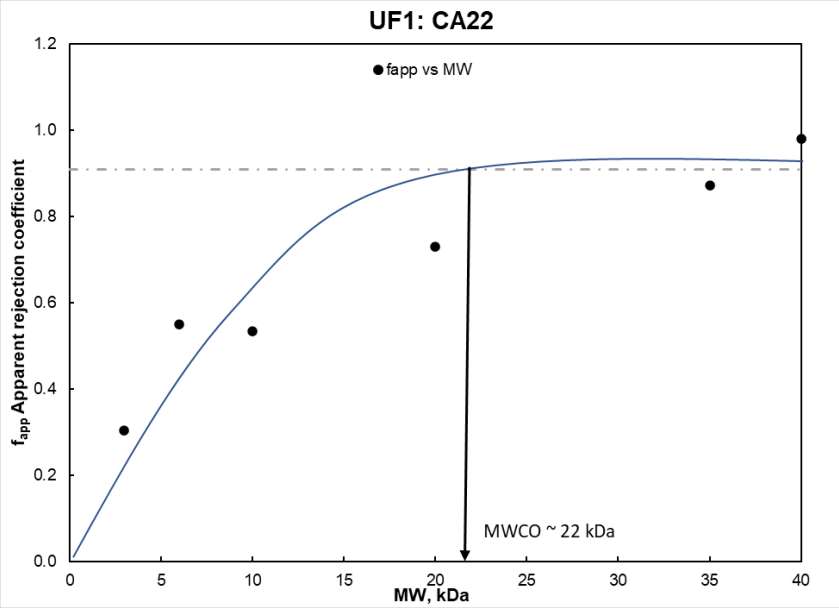

Figure 38- Apparent rejection to PEGs in aqueous solutions with a feed concentration of 0.6 g/L for PEG 3, 6, 10, 20, 35 and 40 kDa at a ΔP_t of 1 bar at the maximum volumetric feed flowrate, Q_F = 3.27 L/min and a membrane surface area, Am, of 13.2 x 10^{-4} m^2 for CA membrane.

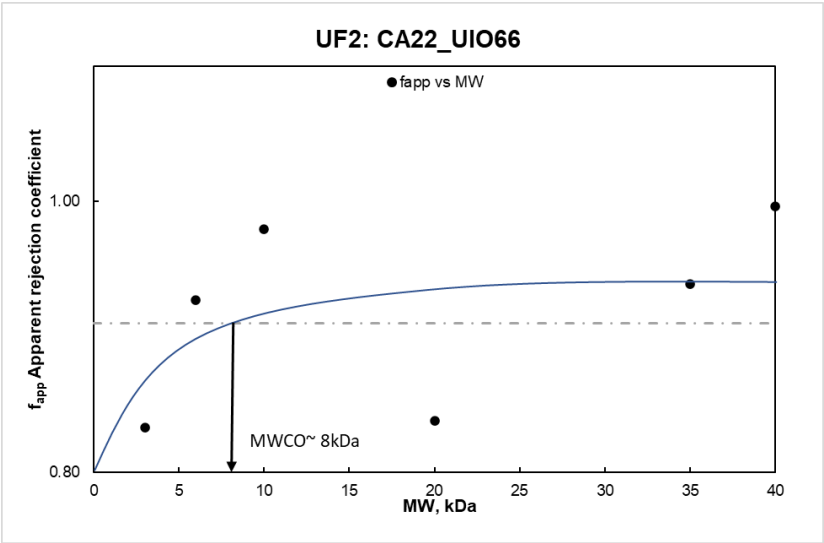

Figure 39- Apparent rejection to PEGs in aqueous solutions with a feed concentration of 0.6 g/L for PEG 3, 6, 10, 20, 35 and 40 kDa at a ΔP_t of 1 bar at the maximum volumetric feed flowrate, Q_F = 3.27 L/min and a membrane surface area, Am, of 13.2 x 10^{-4} m^2 for CA_UiO66 membrane.

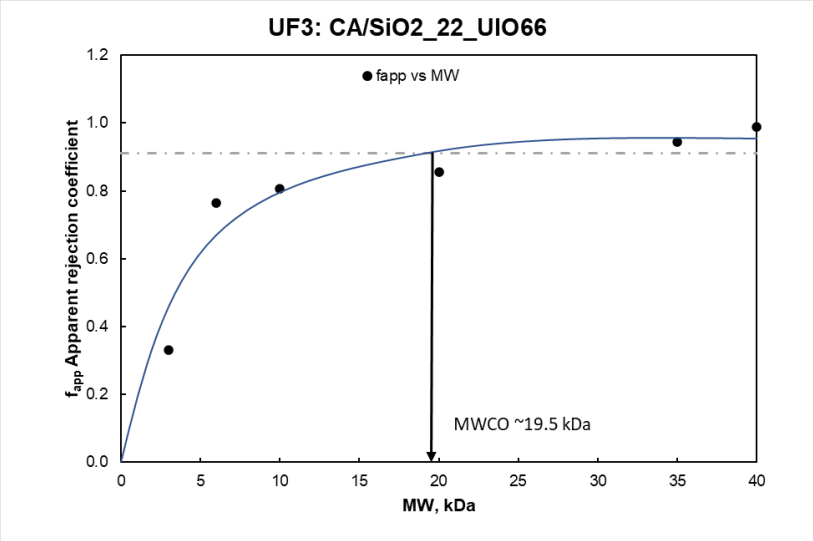

Figure 40- Apparent rejection to PEGs in aqueous solutions with a feed concentration of 0.6 g/L for PEG 3, 6, 10, 20, 35 and 40 kDa at a ΔP_t of 1 bar at the maximum volumetric feed flowrate, Q_F = 3.27 L/min and a membrane surface area, Am, of 13.2 x 10^{-4} m^2 for CA/SiO_2_UiO66 membrane.

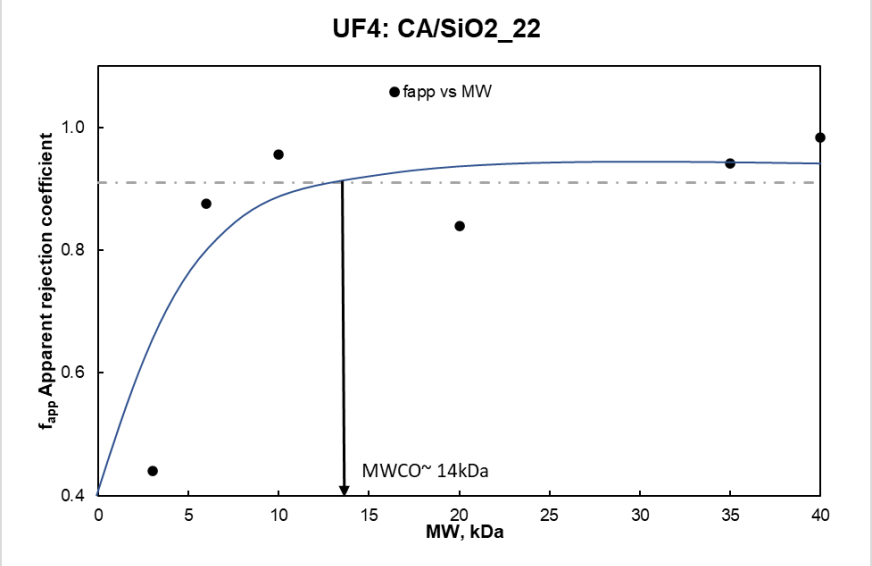

Figure 41- Apparent rejection to PEGs in aqueous solutions with a feed concentration of 0.6 g/L for PEG 3, 6, 10, 20, 35 and 40 kDa at a ΔP_t of 1 bar at the maximum volumetric feed flowrate, Q_F = 3.27 L/min and a membrane surface area, Am, of 13.2 x 10^{-4} m^2 for CA/SiO_2 membrane.

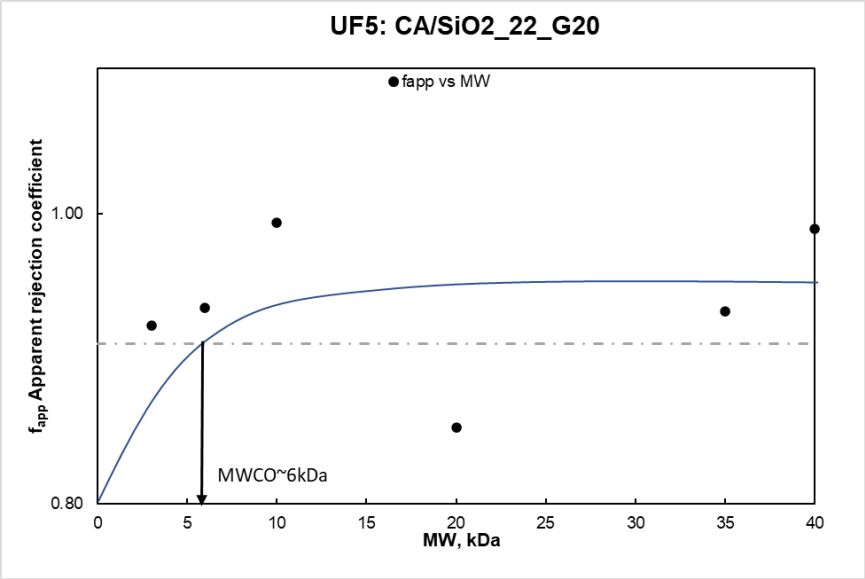

Figure 42- Apparent rejection to PEGs in aqueous solutions with a feed concentration of 0.6 g/L for PEG 3, 6, 10, 20, 35 and 40 kDa at a ΔP_t of 1 bar at the maximum volumetric feed flowrate, Q_F = 3.27 L/min and a membrane surface area, Am, of 13.2x10^{-4} m^2 for CA_UiO66 membrane.

Table 13- Values of Molecular weight Cut off (MWCO) in kDa.

Membrane	MWCO (kDa)
CA	22
CA_UiO66	8
CA/SiO_2	14
CA/SiO_2_UiO66	19.5
CA/SiO_2_G20	6

One more time, the effect of introducing MOF(UiO66) as it can be seen in the CA membrane reduces from 22 kDa to 8 kDa and in CA/SiO_2 membrane increases the MWCO from 14 kDa to 19.5 kDa and it´s also possible to state that UiO66 induced an increase in pore size. The lowest MWCO in this batch for the CA/SiO_2_G20 membrane.

Furthermore, by comparing the MW of small water-soluble compounds (MW< 500 Da) with the MWCO values for each membrane (> 6 kDa), it is possible to anticipate that urea and PCs can be removed when not bound to any protein.

5.2.3 Apparent rejection coefficient to Salts

The apparent rejection coefficients, f (%), of NaCl and Na_2SO_4, were used to assess the selectivity of each membrane. All the permeation experiments were conducted at the maximum volumetric feed flowrate (Q_F= 3.27 L/min), which corresponded to the maximum volumetric velocity. The apparent rejection was determined as mentioned before with solutions of 0.6 g/L at 0.5 bar.

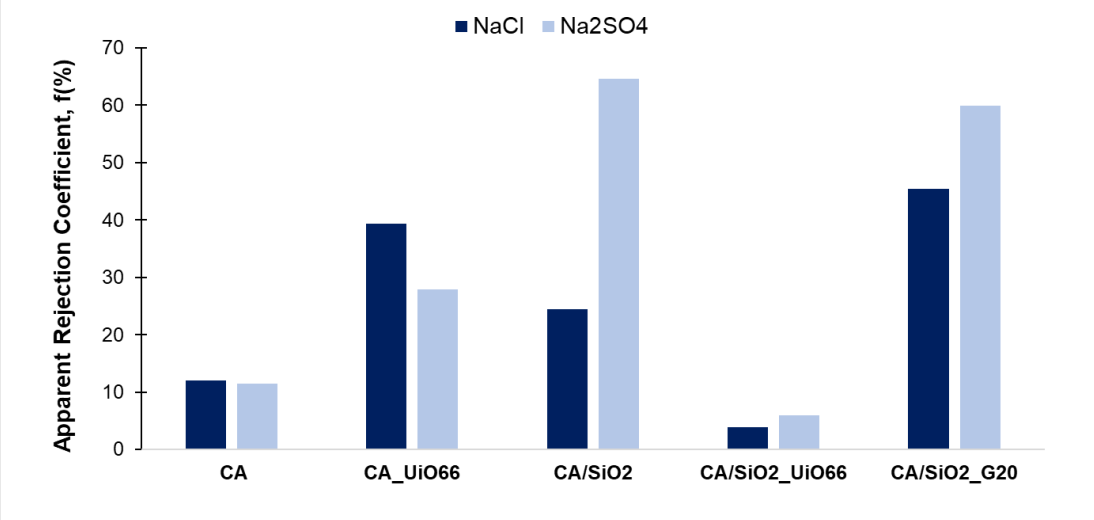

Figure 43-Apparent rejection coefficients (f) in percentage (%), to a monovalent salt, $NaCl$ and bivalent salts, Na_2SO_4 for CA, CA_UiO66, CA/SiO_2_UiO66, CA/SiO_2 and CA/SiO_2_G20 membranes. The f coefficients were determined under total recirculation mode at a transmembrane pressure, ΔP, of 0.5 bar, at maximum volumetric feed flow rate, a membrane surface area of $A_m = 13.2\times10^4$ m^2 a feed solution concentration of 0.6 g/L.

The mass flux permeability of the salts for each membrane was also determined and the values are presented in the table below:

Table 14- Permeate mass fluxes (25 °C) at 0.5 bar of the monovalent salt, NaCl, and divalent salt, Na_2SO_4.

Salts Permeate mass fluxes at 2 5°C (Kg/h.m²) at 0.5 bar		
Membrane	**NaCl**	**Na_2SO_4**

CA	4	4.2
CA_UiO66	0.9	0.8
CA/SiO_2_UiO66	8	8.1
CA/SiO_2	1.7	1.8
CA/SiO_2_G20	0.5	0.4

Through the results above it is possible to conclude that the salts are partially rejected by membranes and the influence of introducing MOF is also seen. the apparent rejection coefficient of CA membrane, f, to salts is lower than CA_UiO66 membrane and CA/SiO_2 membrane is higher than CA/SiO_2_UiO66 membrane.

There´s a significantly difference between the rejection of a monovalent salt and divalent salt in CA/SiO_2 membranes. In CA/SiO_2 and CA/SiO_2_G20 membranes the rejection to Na_2SO_4 is bigger than rejection NaCl.

Regarding the permeate flux, there's not a significant difference between the monovalent salt and the divalent salt, Na_2SO_4.

5.2.4. Apparent rejection coefficient to Uremic toxins

The apparent rejection coefficients, f, were determined over a pressure range from 0.5 to 3 bar for following solutions: 0.4 g/L of Urea, 4.6 g/L of Urea, 0.1 g/ L of p-CS, 0.5 g/L of BSA and 0.5 g/L of PCs and 0.1 g/L of PCs. In these 2 last cases, the apparent rejection refers to P_Cs.

The permeate fluxes of the uremic toxins are represented in **Appendix D.**

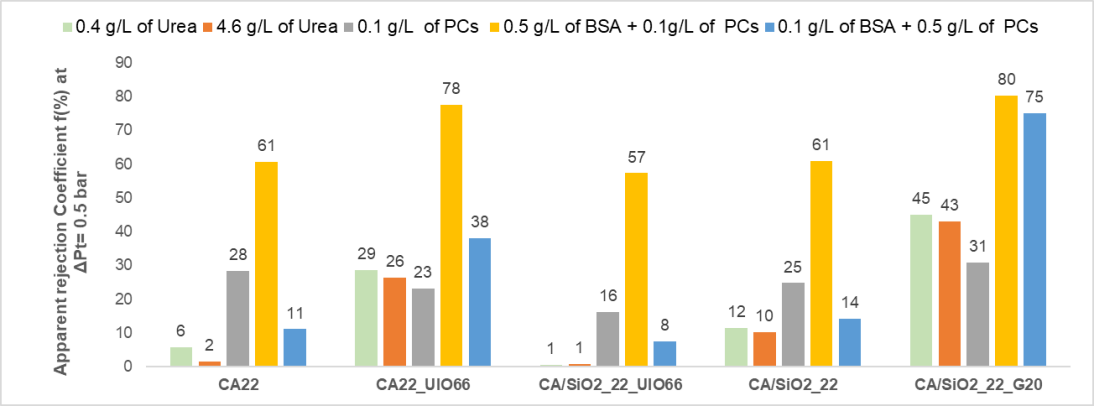

Figure 44 -Apparent rejection coefficient of each membrane to Uremic toxins: Urea, P_cresyl sulfate (PCs), solution with 0.1 g/L of PCs +0.5 g/L of Bovine Serum Albumin (BSA) and solution with 0.5 g/L of PCs and 0.1 g/L of Bovine Serum Albumin (BSA) apparent rejection coefficients this last solutions refers to PCs the solutions at transmembrane pressure (ΔP_t) of 0.5 bar. The f coefficients were determined under total recirculation mode at, at maximum volumetric feed flow rate, a membrane surface area of $A_m = 13.2\times10^4$ m^2.

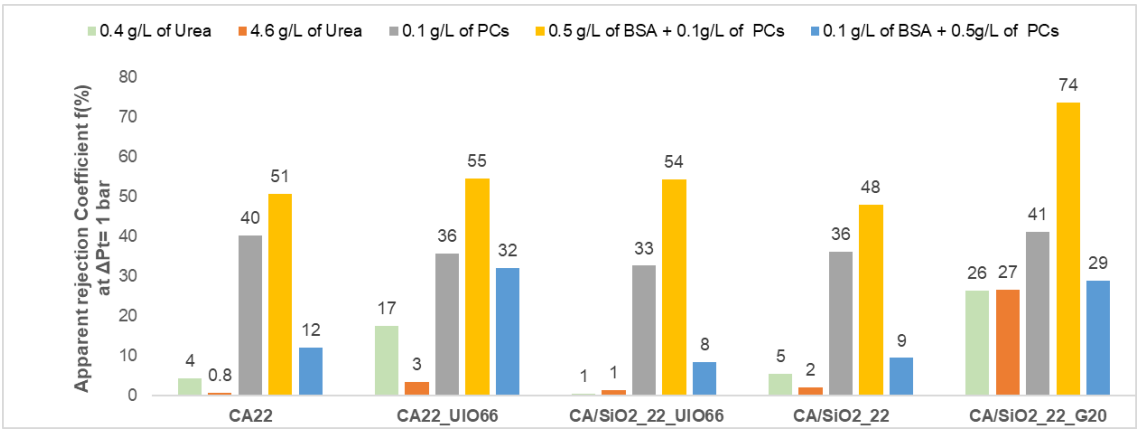

Figure 45- Apparent rejection coefficient of each membrane to Uremic toxins: Urea, P_Cresyl sulfate (PCs), solution with 0.1 g/L of p-CS +0.5 g/L of Bovine Serum Albumin (BSA) and solution with 0.5 g/L of p-CS and 0.1 g/L of Bovine Serum Albumin (BSA) at transmembrane pressure(ΔP_t) of 1 bar. The f coefficients were determined under total recirculation mode, at maximum volumetric feed flowrate (Q_F = 3.27 L/min), a membrane surface area of $A_m = 13.2\times10^4$ m^2.

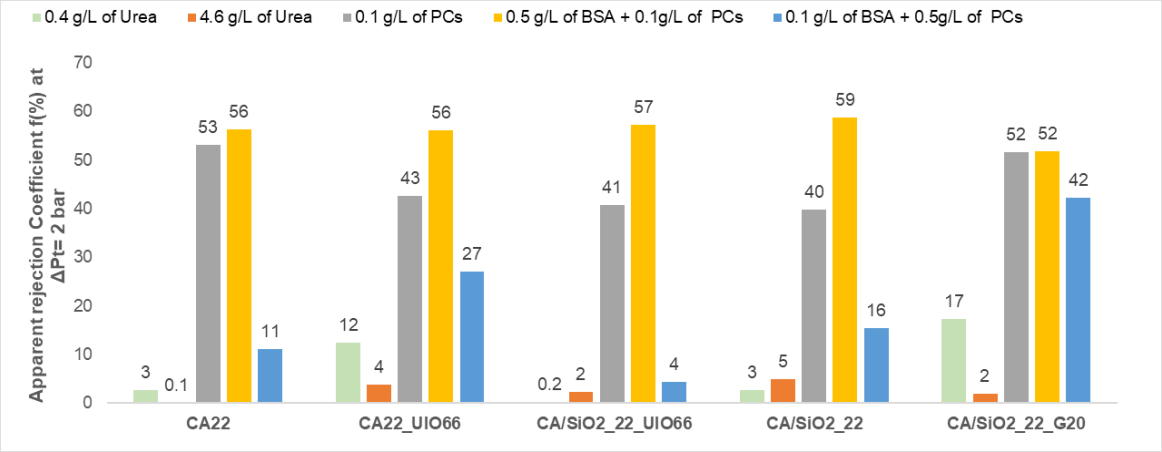

Figure 46- Apparent rejection coefficient of each membrane to Uremic toxins: Urea, P_Cresyl sulfate (PCs), solution with 0.1 g/L of p-CS +0.5 g/L of Bovine Serum Albumin (BSA) and solution with 0.5 g/L of p-CS and 0.1 g/L of Bovine Serum Albumin (BSA) at transmembrane pressure(ΔP_t) of 2 bar. The f coefficients were determined under total recirculation mode, at maximum volumetric feed flowrate (Q_F = 3.27 L/min) , a membrane surface area of $A_m = 13.2\times10^4$ m^2.

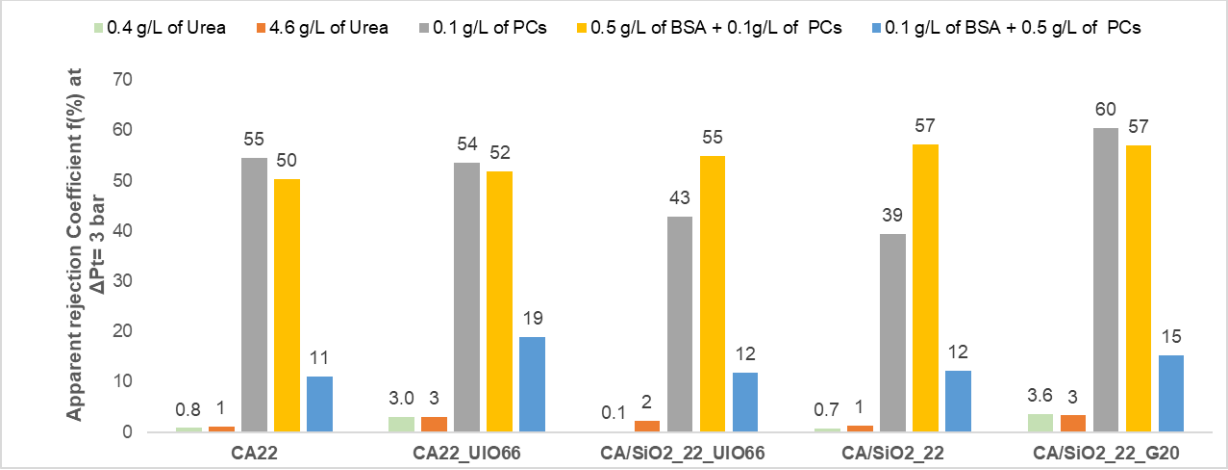

Figure 47- Apparent rejection coefficient of each membrane to Uremic toxins: Urea, P_Cresyl sulfate (PCs), solution with 0.1 g/L of PCs +0.5 g/L of Bovine Serum Albumin (BSA) and solution with 0.5 g/L of PCs and 0.1 g/L of Bovine Serum Albumin (BSA) at transmembrane pressure (ΔP_t) of 3 bar. The f coefficients were determined under total recirculation mode, at maximum volumetric feed flowrate (Q_F=3.27 L/min), a membrane surface area of $A_m = 13.2\times10^4$ m^2.

As it can see from Figure 44 to Figure 47, The apparent rejections of CA, CA/SiO_2 and CA/SiO_2_UiO66 membranes to the Urea solution(0.4 g/L and 4.6 g/L) are very low ,i.e. there is practically no rejection. As expected, Urea permeation gives low rejections, because as

mentioned before, Urea is considered a small water-soluble compound (MW < 500) [5,6] with MW of 60 Da. In other hand, for CA/SiO_2_G20 and CA_UiO66 membrane the rejections to Urea are relatively high, principally in lowers transmembrane pressures.

In case of PCs is possibles to see the effect of transmembrane and that the apparent rejections of these membranes to this uremic toxin are higher comparing with Urea permeation. It can also be seen the effect of introducing MOF in CA membrane. The apparent rejection to Urea increases by adding UiO66 in CA membrane, it clearly seen immediately at the transmembrane pressure of 0.5 bar.

Relative to the last 2 two scenarios where PCs is binding with BSA, in the first stage (0.1 g/L of PCs with 0.5 g/L BSA) the apparent rejection of PCs are also higher comparing with the permeation of PCs solution only. Moreover, in case of another scenario (0.5 g/L of PCs with 0.1 g/L of BSA), the apparent rejection coefficients (f) are lower than the first stage. This decrease of apparent rejection is expected, because in the last case there are biggest free fraction of PCs, so the rejection decreases.

6. Conclusions

CA membrane and CA/SiO_2 membranes were successfully synthesized by combining phase inversion and sol-gel techniques. Additionally, MOF-UiO66 was incorporated by direct dispersion method. CA and CA/SiO_2 membranes were subjected to post-treatment using surfactant as aqueous solutions of glycerol (20%) (G20) or aqueous solution of triton-X-100 (4%) and glycerol (20%) (GT).

By differential scanning calorimetry (DSC) it was shown that, on cooling, most of water recrystallizes at temperatures close to -18 °C, as expected for bulk water. On the other side, water evaporation depends on the membrane, occurring at approximately 30 degrees below for CA/SiO_2 and CA_UiO66 membranes relative to CA. In the post-treated membranes, there is no signal of bulk water recrystallization on cooling (and on heating).

Relatively to the crystallinity degree it depends on the membrane composition following this order: CA/SiO_2 (28%), CA (14%), CA/SiO_2_UiO66 (10%) and CA_UiO66 (8%). Regarding the glass transition temperature, it is almost unaffected by the presence of SiO_2 and/or UiO66; on the other hand, it is shifted to lower values when CA are fully amorphous. The presence of glycerol and/or triton-X-100 does not significantly change the glass transition and the melting enthalpy is extremely higher than untreated membranes.

The molecular mobility was probed by dielectric relaxation spectroscopy (DRS). The main result refers to the reduction of the number of relaxation modes observed at lower temperatures, that changes from five detected in CA to three observed in hybrid membranes with or without UiO66. These relaxations are principally related to the water presence in the samples, given that after heating above 250 °C, both number and intensity are significantly depleted in all studied membranes. All the detected relaxations follow an Arrhenius temperature dependence of the corresponding relaxation times. In the post-treated membranes, the dynamical signature of the glass transition of glycerol is clearly observed probing that this compound keeps in the membranes after post-treatment.

Regarding the me membrane selective analysis, the incorporation of UiO66 decreases the L_p of the CA based membrane from 10 to 3 Kg/(h.m^2.bar) and increases the L_p of the CA/SiO_2 membrane from 4 to 22 Kg/(h.m^2.bar). The CA/SiO_2_G20 holds the lowest hydraulic permeability (2 Kg/(h.m^2.bar)).

The incorporation of UiO66 decreases the MWCO of the CA membrane from 22 to 8 kDa and increases the MWCO of the CA/SiO_2 based membrane from 14 to 19.5 kDa. The CA/SiO_2_G20 membrane holds the lowest value of MWCO, 6 kDa.

Regarding the salts permeation, the incorporation of UiO66 results to higher salt rejection coefficients for CA based membrane and to lower salt rejection coefficients for the CA/SiO_2 membranes. CA/SiO_2 and CA/SiO_2_G20 membranes displays higher rejection coefficients to Na_2SO_4 to NaCl.

The lowest coefficients to Urea and P_Cresyl sulfate are displayed by the CA/SiO_2_UiO66 membrane.

In BSA/P_cresyl sulfate solutions the rejection coefficients to p_cresyl sulfate are very high when the BSA concentration is higher, and they decrease drastically when BSA concentration is lower.

6. Perspective of Future works

- Characterization methods such as Scanning Electron Microscopy (SEM), X-Ray Photoelectron (XRP), Nuclear Magnetic Resonance (NMR) to show the presence of SiO_2 and UiO66.
- FTIR, to see the interactions regarding UiO66 and Glycerol.

8.References:

[1] Liyanage, T., Ninomiya, T., Jha, V., Neal, B., Patrice, H. M., Okpechi, I., Zhao, M. H., Lv, J., Garg, A. X., Knight, J., Rodgers, A., Gallagher, M., Kotwal, S., Cass, A., & Perkovic, V. (**2015**). Worldwide access to treatment for end-stage kidney disease: a systematic review. The Lancet, 385(9981), 1975-1982. doi: 10.1016/S0140-6736(14)61601-9.

[2] Hill, N. R., Fatoba, S. T., Oke, J. L., Hirst, J. A., O'Callaghan, C. A., Lasserson, D. S., Hobbs, F. D. R., & Remuzzi, G. (**2016**). Global Prevalence of Chronic Kidney Disease – A Systematic Review and Meta-Analysis. PLOS ONE, 11(7), e0158765. doi: 10.1371/journal.pone.0158765.

[3] Zaman, S. U., Rafiq, S., Ali, A., Mehdi, M. S., Arshad, A., Rehman, S. U., Muhammad, N., Irfan, M., Khurram, M. S., Zaman, M. K. U., Hanbazazah, A. S., Lim, H. R., & Show, P. L. (**2022**). Recent advancement challenges with synthesis of biocompatible hemodialysis membranes. Chemosphere, 307(2), 135626. doi: 10.1016/j.chemosphere.2022.135626.

[4] Meijers, B. K. I., Bammens, B., Verbeke, K., & Evenepoel, P. (**2008**). A Review of Albumin Binding in CKD. American Journal of Kidney Diseases, 51(5), 839-850. doi: 10.1053/j.ajkd.2007.12.035.

[5] Faria, M., & de Pinho, M. N. (**2021**). Challenges of reducing protein-bound uremic toxin levels in chronic kidney disease and end stage renal disease. Translational Research, 229, 115-134. doi: 10.1016/j.trsl.2020.09.001.

[6] Vanholder, R., De Smet, R., Glorieux, G., Argilés, A., Baurmeister, U., Brunet, P., Clark, W., Cohen, G., De Deyn, P. P., Deppisch, R., Descamps-Latscha, B., Henle, T., Jörres, A., Lemke, H. D., Massy, Z. A., Passlick-Deetjen, J., Rodriguez, M., Stegmayr, B., Stenvinkel, P., Tetta, C., Wanner, C., & Zidek, W. (**2003**). Review on uremic toxins: Classification, concentration, and interindividual variability. Kidney International, 63(5), 1934–1943. doi: 10.1046/j.1523-1755.2003.00924.x

[7] Daugirdas, J. T., Blake, P. G., & Ing, T. S. (**2012**). Handbook of Dialysis. Lippincott Williams & Wilkins. doi: 10.1093/ndt/gfm195.

[8] El Gen Curioso. (n.d.). Sistema Urinario - Diccionario., [accessed on May,06], from https://www.elgencurioso.com/diccionario/sistema-urinario/.

[9] Bungay, P. M., Lonsdale, H. K., & de Pinho, M. N. (**1986**). Synthetic Membranes: Science, Engineering and Applications. Dordrecht: Springer Netherlands, 1389-2185. doi: 10.1007/978-94-009-4712-2.

[10] Mulder, M. (**1991**). Basic Principles of Membrane Technology. Dordrecht: Springer Netherlands. doi: 10.1007/978-94-017-0835-7.

[11] Porter, M. C. (**1990**). Handbook of Industrial Membrane Technology. Westwood, NJ: Noyes Publications.

[12] Singh, R. (**2005**). Water and membrane treatment. Hybrid Membrane Systems for Water Purification, 1, 57-130.

[13] Abdullah, N., Rahman, M. A., Othman, M. H. D., Jaafar, J., & Ismail, A. F. (**2018**). Membranes and Membrane Processes. In Current Trends and Future Developments on (Bio) Membranes, 45-70. Elsevier. doi: 10.1016/B978-0-12-813549-5.00002-5.

[14] Hsieh, H. P. (**1991**). Inorganic Membrane Reactors. Catalysis Reviews, 33(1-2), 1-70. doi: 10.1080/01614949108020296.

[15] Jamil, S. M., Othman, M. H. D., Rahman, M. A., Jaafar, J., Ismail, A. F., & Li, K. (**2015**). Recent fabrication techniques for micro-tubular solid oxide fuel cell support: A review. Journal of the European Ceramic Society, 35(1), 1-22. doi: 10.1016/j.jeurceramsoc.2014.08.034.

[16] Cross Flow Membrane Operations. (**2014**, July 22). Retrieved from https://synderfiltration.com/learning-center/articles/module-configurationsprocess/cross-flow-membrane-operations/(acessed on May,06).

[17] Dead end vs cross flow filtration schema. (n.d.). Retrieved from http://www.zena-membranes.cz/index.php/gallery/othergalery (acessed on May,06).

[18] Schmeling, N., Konietzny, R., Sieffert, D., Rölling, P., & Staudt, C. (**2010**). Functionalized copolyimide membranes for the separation of gaseous and liquid mixtures. Beilstein Journal of Organic Chemistry, 6, 789-800. doi:10.3762/bjoc.6.86.

[19] Gohil, J. M., & Choudhury, R. R. (**2019**). Introduction to Nanostructured and Nano-enhanced Polymeric Membranes: Preparation, Function, and Application for Water Purification. In Nanoscale Materials in Water Purification,25-57. Elsevier. doi: 10.1016/B978-0-12-813926-4.00038-0.

[20] Pinho, M. (**2019**). Separation of Functional Molecules in Food by Membrane Technology. Introduction in Membrane Technologies. In Introduction in Membrane Technologies, 1-29. doi: 10.1016/B978-0-12-815056-6.00001-2.

[21] Porter, M. C. (**1990**). Handbook of Industrial Membrane Technology. Westwood, NJ: Noyes Publications.

[22] Sidney, L., Sourirajan, S. (**1963**). Saline Water Conversio. Washington, D.C.: American Chemical Society. doi: 10.1021/ba-1963-0038.

[23] Abdullah, N. (**2018**). Membranes and Membrane Processes. In Current Trends and Future Developments on (Bio) Membranes ,45-70. doi: 10.1016/B978-0-12-813549-5.00002-5.

[24] Cassano, A., Conidi, C., Ruby-Figueroa, R., & Castro-Muñoz, R. (**2018**). Nanofiltration and Tight Ultrafiltration Membranes for the Recovery of Polyphenols from Agro-Food By-Products. International Journal of Molecular Sciences, 19(2), 351.doi:10.3390/ijms19020351.

[25] Brinker, J., Scherer, G. (**1990**). Sol-Gel Science: The Physics and Chemistry of Sol-Gel Processing. Retrieved from the publisher's website or database. doi: 1016/C2009-0-22386-5.

[26] Levy, D., Zayat, M. (Eds.) (**2015**). The Sol-Gel Handbook: Synthesis, Characterization, and Applications. Weinheim: Wiley-VCH.

[27] Aegerter, M. A., & Mennig, M. (Eds.). (**2004**). Sol-Gel Technologies for Glass Producers and Users. Boston, MA: Springer US. doi: 10.1007/978-0-387-88953-5.

[28] Cheng, Z., Wang, Z., & Zhao, D. (**2018**). Mixed Matrix Membranes for Natural Gas Upgrading: Current Status and Opportunities. Industrial & Engineering Chemistry Research, 57(12), 4139-4169. doi: 10.1021/acs.iecr.7b04796.

[29] Park, H. B., Kamcev, J., Robeson, L. M., Elimelech, M., & Freeman, B. D. (**2017**). Maximizing the right stuff: The trade-off between membrane permeability and selectivity. Science, 356(6343), doi: 10.1126/science. aab0530.

[30] Monsalve-Bravo, G., & Bhatia, S. (**2018**). Modeling Permeation through Mixed-Matrix Membranes: A Review. Processes, 6(9), 172. doi: 10.3390/pr6090172.

[31] Ha, H., Park, J., Ando, S., Kim, C. B., Nagai, K., Freeman, B. D., & Ellison, C. J. (**2016**). Gas Permeation and Selectivity of Poly(dimethylsiloxane)/Graphene Oxide Composite Elastomer Membranes. Journal of Membrane Science, 518, 131-140. doi: 10.1016/j.memsci.2016.06.028.

[32] Ha, H., Park, J., Ha, K., Freeman, B. D., & Ellison, C. J. (**2016**). Synthesis and gas permeability of highly elastic poly(dimethylsiloxane)/graphene oxide composite elastomers using telechelic polymers. Polymer, 93, 53-60. doi: 10.1016/j.polymer.2016.04.016.

[33] Geremia, I., Jong, J. A. W., van Nostrum, C. F., Hennink, W. E., Gerritsen, K. G. F., & Stamatialis, D. (**2021**). New mixed matrix membrane for the removal of urea from dialysate solution. Separation and Purification Technology, 277, 119-408. doi: 10.1016/j.seppur.2021.119408.

[34] Yin, J., & Deng, B. (2015). Polymer-matrix nanocomposite membranes for water treatment. Journal of Membrane Science, 479, 256-275. doi: 10.1016/j.memsci.2014.11.019.

[35] Vanholder, R., De Smet, R., & Glorieux, G. (**2003**). Review on uremic toxins: Classification, concentration, and interindividual variability. Kidney International, 63, 1934-1943.

[36] Yu, S., Schuchardt, M., Tölle, M., van der Giet, M., Zidek, W., Dzubiella, J., & Ballauff, M. (**2017**). Interaction of human serum albumin with uremic toxins: a thermodynamic study. RSC Advances, 7, 27913-27922.

[37] Hulme, E. C., & Trevethick, M. A. (**2010**). Ligand binding assays at equilibrium: validation and interpretation. British Journal of Pharmacology, 161(6), 1219-1237.

[38] Jansen, J., Jankowski, J., Gajjala, P. R., Wetzels, J. F. M., & Masereeuw, R. (**2017**). Disposition and clinical implications of protein-bound uremic toxins. Clinical Science, 131(14), 1631-1647. doi:10.1042/CS20160191.

[39] Viaene, L., Annaert, P., de Loor, H., Poesen, R., Evenepoel, P., & Meijers, B. (**2013**). Albumin is the main plasma binding protein for indoxyl sulfate and p-cresyl sulfate. Biopharmaceutics & Drug Disposition, 34(3), 165-175.

[40] Sakai, T., Takadate, A., & Otagiri, M. (**1995**). Characterization of binding site of uremic toxins on human serum albumin. Biological and Pharmaceutical Bulletin, 18(12), 1755-1761.
[41] Mondal, M., Lakshmi, P., Krishna, R., & Sakthivel, N. (**2017**). Molecular interaction between human serum albumin (HSA) and phloroglucinol derivative that show selective anti-proliferative potential. Journal of Luminescence, 192, 431-437. doi: 10.1016/j.jlumin.2017.08.007.

[42] Daneshamouz, S., Ubong, E., & Abdelrasoul, A. (**2021**). Protein-bound uremic toxins (PBUTs) in chronic kidney disease (CKD) patients: Production pathway, challenges, and recent advances in renal PBUTs clearance. NanoImpact, 1-9. doi: 10.1016/j.impact.2021.100299.

[43] Yang, Q., Zhang, H.-Y., Wang, L., Zhang, Y., & Zhao, J. (**2018**). Ru/UiO-66 Catalyst for the Reduction of Nitroarenes and Tandem Reaction of Alcohol Oxidation/Knoevenagel Condensation. ACS Omega, 3(4), 4199-4212. doi: 10.1021/acsomega.8b00157.

[44] Morelli Venturi, D., Campana, F., Marmottini, F., Costantino, F., & Vaccaro, L. (**2020**). Extensive Screening of Green Solvents for Safe and Sustainable UiO-66 Synthesis. ACS Sustainable Chemistry & Engineering, 8(46), 17154–17164. doi:10.1021/acssuschemeng.0c05587.

[45] Winarta, J., Shan, B., McIntyre, S. M., Ye, L., Wang, C., Liu, J., & Mu, B. (**2019**). A Decade of UiO-66 Research: A Historic Review of Dynamic Structure, Synthesis Mechanisms, and Characterization Techniques of an Archetypal Metal–Organic Framework. Crystal Growth & Design,20(2), 1347–1362. doi: 10.1021/acs.cgd.9b00955.

[46] Valenzano, L., Civalleri, B., Chavan, S., Bordiga, S., Nilsen, M. H., Jakobsen, S., & Lillerud, K. P. (**2011**). Disclosing the Complex Structure of UiO-66 Metal Organic Framework: A Synergic Combination of Experiment and Theory. Chemistry of Materials, 23(7), 1700-1718. doi: 10.1021/cm1022882.

[47] Dedecker, K., Pillai, R. S., Nouar, F., Pires, J., Steunou, N., Dumas, E., & Pinto, M. L. (**2020**). Metal-Organic Frameworks for Cultural Heritage Preservation: The Case of Acetic Acid Removal. Chemical Reviews, 120(16), 8760-8786. doi: 10.1021/acs.chemrev.9b007.

[48] Feigenbaum, J., & Neuberg, C. A. (1941). Simplified Method for the Preparation of Aromatic Sulfuric Acid Esters. Journal of the American Chemical Society, 63(12), 3529–3530. doi:10.1021/ja01857a508.

[49] Deng, Y., Wu, Y., Chen, G., Zheng, X., Dai, M., & Peng, C. (**2021**). Metal-organic framework membranes: Recent development in the synthesis strategies and their application in oil-water separation. Chemical Engineering Journal, 405, 127004. doi: 10.1016/j.cej.2020.127004.

[50] Mendes, G., Faria, M., Carvalho, A., Gonçalves, M. C., & de Pinho, M. N. (2018). Structure of water in hybrid cellulose acetate-silica ultrafiltration membranes and permeation properties. Carbohydrate Polymers, 189, 342-351. doi: 10.1016/j.carbpol.2018.02.031.

[51] Brinker, C. J., & Scherer, G. W. (**1990**). Sol-Gel Science. San Diego: Academic Press.

[52] Mendes, G. (**2016**). Novas Membranas Assimétricas de Matriz Mista de Acetato de Celulose e Sílica [New Asymmetric Membranes of Mixed Matrix of Cellulose Acetate and Silica]. Instituto Superior Técnico, Universidade de Lisboa.

[53] Andrade, M. C., Pereira, J. C., de Almeida, N., Marques, P., Faria, M., & Gonçalves, M. C. (**2021**). Improving hydraulic permeability, mechanical properties, and chemical functionality of cellulose acetate-based membranes by co-polymerization with tetraethyl orthosilicate and 3-(aminopropyl)triethoxysilane. Carbohydrate Polymers, 261, 117813. doi: 10.1016/j.carbpol.2021.117813.

[54] Sidney, L., & Sourirajan, S. (**1963**). Saline Water Conversion—II (38). Washington, D. C.: American Chemical Society. doi: 10.1021/ba-1963-0038.

[55] Scott, K. (**1995**). Handbook of industrial membranes (1st ed.). Oxford: Elsevier Advanced Technology.

[56] Moore, T. T., & Koros, W. J. (**2005**). Non-ideal effects in organic–inorganic materials for gas separation membranes. Journal of Molecular Structure, 739(1–3), 87–98.doi: 10.1016/j.molstruc.2004.05.043.

[57] Kesting, R. E., & Menefee, A. (**1969**). The role of formamide in the preparation of cellulose acetate membranes by the phase inversion process. Kolloid-Z.u.Z.Polymere, 230(2), 341–346. doi: 10.1007/BF01520608.

[58] Vos, D., & Burris, F. O. (1969). Drying cellulose acetate reverse osmosis membranes. Industrial & Engineering Chemistry Product Research and Development, 8(1), 84–89. doi: 10.1021/I360029A016

[59] Brites, A. M. (**1991**). Modelação de Processos de Transporte em Ultrafiltração [Modeling of Transport Processes in Ultrafiltration].

[60] Rosa, M. J. (**1995**). Separação Seletiva de Compostos Orgânicos de Correntes Aquosas por Ultrafiltração e Nanofiltração [Selective Separation of Organic Compounds from Aqueous Streams by Ultrafiltration and Nanofiltration].

[61]Lonsdale, H. K., Merten, U., & Riley, R. L. (**1965**). Transport properties of cellulose acetate osmotic membranes. Journal of Applied Polymer Science, 9(4), 1341–1362. doi:10.1002/app.1965.070090413.

[62] Wiford, R. J. (**2021**, June 15). How to Calculate Transmembrane Pressure. Membrane System Specialists, Inc. Retrieved August 21, 2022, from https://www.mssincorporated.com/blog/howto-calculate-transmembrane-pressure/(acessed on May, 06)

[63] Singh, R. (**2005**). Water and membrane treatment. Hybrid Membrane Systems for Water Purification, 1, 57-130.

[64] Mulder, M. (**1991**). Basic Principles of Membrane Technology. Dordrecht: Springer Netherlands. doi:10.1007/978-94-017-0835-7.

[65] da Silva, M. P. (**2019**). Tailoring the selective permeation properties of asymmetric cellulose acetate/Silica Hybrid Membranes and characterization of water dynamic in hydrated membranes by Deuterium nuclear magnetic resonance.

[66] Amin, N., Mahmood, R. T., Asad, M., & Noorulamin, M. (**2014**). Evaluating Urea and Creatinine Levels in Chronic Renal Failure Pre and Post Dialysis: A Prospective Study. 2, 2330-4596.

[67] Falconi, C. A., Junho, C. V. D. C., Fogaça-Ruiz, F., Vernier, I. C. S., da Cunha, R. S., Stinghen, A. E. M., & Carneiro-Ramos, M. S. (**2021**). Uremic Toxins: An Alarming Danger Concerning the Cardiovascular System. Frontiers in Physiology, 12, 686249. doi: 10.3389/fphys.2021.686249.

[68]] El Khaled, D., Castellano, N. N., Gázquez, J. A., Perea-Moreno, A.-J., & Manzano-Agugliaro, F. (**2016**). Dielectric Spectroscopy in Biomaterials: Agrophysics. Materials, 9, 310. doi: 10.3390/ma9050310.

[69]Note, A. (**2007**). Agilent Basics of Measuring the Dielectric Properties of Materials. Measurement Techniques, 50(3), 227–231.

[70] Franco, A. I. (**2018**). Stabilizing High Energetic States of Pharmaceutical Drugs ,105.

[71] Havriliak, S. & Negami, S. (**1967**). A complex plane representation of dielectric and mechanical relaxation processes in some polymers. Polymer, 8, 161–210. doi: 10.1016/0032-3861(67)90021-3.

[72] Havriliak, S., & Negami, S. (1966). A complex plane analysis of α-dispersions in some polymer systems. Journal of Polymer Science Part C: Polymer Symposia, 14, 99–117. doi:10.1002/polc.5070140111.

[73] High-Tech Science Corporation. (n.d.). Introducing the Temperature Modulated DSC, 52.

[74] http://the-dielectric-society.org/sites/default/files/williams2005.pdf. (Accessed on May,06).

[75] Kodre, K. V., Attarde, S. R., Yendhe, P. R., Patil, R. Y., & Barge, V. U. (**2014**). Differential Scanning Calorimetry: A Review. Research Reviews: Journal of Pharmaceutical Analysis, 3, 11-22.
[76] High-Tech Science Corporation, H. Introducing the Temperature Modulated DSC ,52.

[77] Reading, M., Luget, A., & Wilson, R. (**1994**). Modulated differential scanning calorimetry. Thermochimica Acta, 238, 295-307. doi: 10.1016/S0040-6031(94)85215-4.

[78] https://www.ru.nl/science/gi/facilitiesactivities/elemental-analysis/toc(acessed on May,06).

[79] Settle, F. A. (Ed.). (**1997**). Handbook of Instrumental Techniques for Analytical Chemistry. doi:10.1080/10826079808006889.

[80] Barron, J. J., & Ashton, C. (**2013**). The effect of temperature on conductivity measurement.

[81] Perkampus, H. (**1992**). UV-VIS Spectroscopy and Its Applications. Berlin, Heidelberg: Springer Berlin Heidelberg.doi:0.1007/978-3-642-77477-5.

[82] Silbey, R. J., Alberty, R. A., & Bawendi, M. G. (**2005**). Physical Chemistry (4th ed.). Hoboken, NJ, USA: John Wiley & Sons, Inc.

[83] Skoog, D. A., Holler, F. J., & Crouch, S. R. (**2007**). Principles of Instrumental Analysis (6th ed.). Belmont, CA: Brooks/Cole.

[84] Cerqueira, D. A., Rodrigues Filho, G., & Assunção, R. M. N. (**2006**). A New Value for the Heat of Fusion of a Perfect Crystal of Cellulose Acetate. Polymer Bulletin, 56, 475.

[85] Sousa, M., Brás, A. R., Veiga, H. I. M., Ferreira, F. C., de Pinho, M. N., Correia, N. T., & Dionísio, M. (**2010**). Dynamical Characterization of a Cellulose Acetate Polysaccharide. The Journal of Physical Chemistry B, 114(34), 10939–10953. doi:10.1021/jp101665h.

[86] Kamide, K. (**2005**). Cellulose and cellulose derivatives: Molecular characterization and its applications. Elsevier: The Netherlands.

[87] Martins, T. D., Viciosa, M. T., Oliveira, M. B., Fernandes, A., Mano, J. F., Baleizão, C., & Farinha, J. P. S. (**2023**). Reversible imine crosslinking in waterborne self-healing polymer coatings.

[88] Vogel, H. (**1921**). Das Temperatur Abhängigkeitsgesetz der Viskosität von Flüssigkeiten. Physikalische Zeitschrift, 22, 645-646.

[89] Böhmer, K. L., Ngai, C. A., Angell, D. J., & Plazek, D. (**1993**). Nonexponential relaxations in strong and fragile glass formers. Journal of Chemical Physics, 99, 4201-4209.doi: 10.1063/1.466117.

[90] Ryabov, Ya. E., Hayashi, Y., Gutina, A., & Feldman, Y. (**2003**). Features of supercooled glycerol dynamics. Physical Review B, 67(13), 132-202. doi:10.1103/PhysRevB.67.132202.

9. Appendix

Appendix A: Temperature Correction of the Permeate Fluxes

All the solutions used in the permeation studies were dilute enough to be classified as water.

However, the density and viscosity of water are: ρ=997.077 kg/m^2 and μ= 0.8949× 10^{-3} 1/m.s respectively.

The viscosity (× 10^{-3} $kgm^{-1}s^{-1}$) is given as function of temperature by these following correlations:

$\ln(\mu) = -6.96 + \frac{2044}{T}$	$287.15 < T(K) < 308.15$
$\ln(\mu) = -6.78 + \frac{1983}{T}$	$287.15 < T(K) \leq 318.15$
$\ln(\mu) = -6.01 + \frac{1749}{T}$	$313.15 < T(K) \leq 333.15$

Knowing: $J_W = L_P \times \Delta P_t$, in terms of J_m, permeate mass flux, in the following form:

$$J_m = \rho \frac{L_p^*}{\mu} \Delta P$$

Moreover, Nether Lp nether ΔP depends on temperature:

$$\frac{J_m(T)\mu(T)}{\rho(T)} = L_P^* \times \Delta P$$

It was possible to correlate the permeate fluxes with different temperature through the following equation:

$$\frac{J_{m1}\mu_1}{\rho_1} = \frac{J_{m2}\mu_2}{\rho_2}$$

In this case in order to $J_{m2}(J_m^{25^\circ C})$:

$$J_{m2} = \frac{\rho_2 J_{m1}\mu_1}{\rho_1 \mu_2}$$

Where J_{m2} , μ_2, ρ_2 corresponds to: $J_m^{25^\circ C}, \mu^{25^\circ C}, \rho^{25^\circ C}$ respectively.

Appendix B: Calibration Curve (Rotameter calibration)

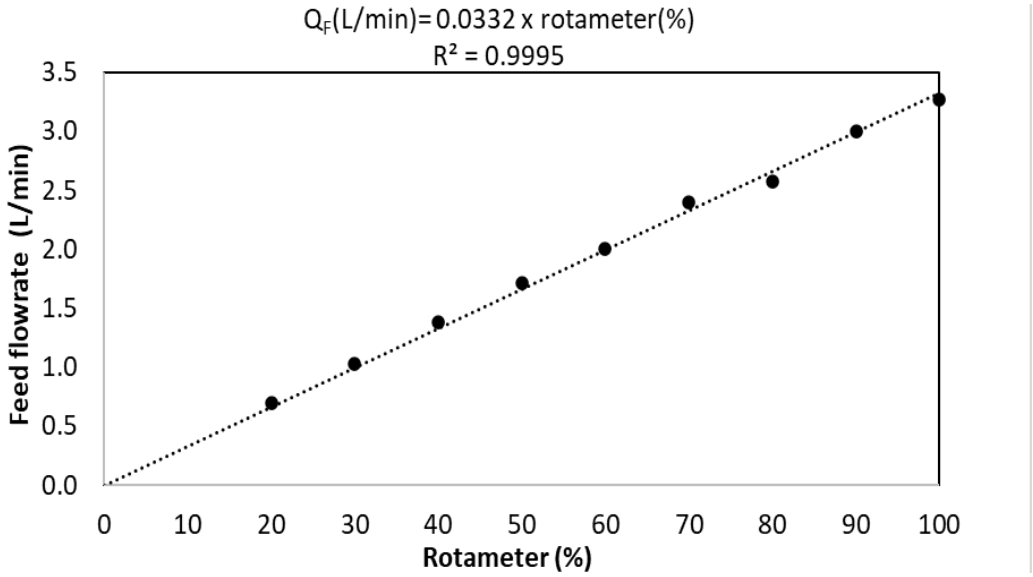

Figure 48- Calibration curve of Rotameter with pure water flowrate(L/min), as a function of rotameterscale, in rot (%). The equation is the result of a linear fit: $Q_F = 0.033 \times Rotameter(\%)$, with the respective coefficient of correlation, R^2=0.99.

Appendix C- TOC calibration curves of Uremic toxins

Appendix C.1-Calibration curve of P_CS by US-Vis spectroscopy

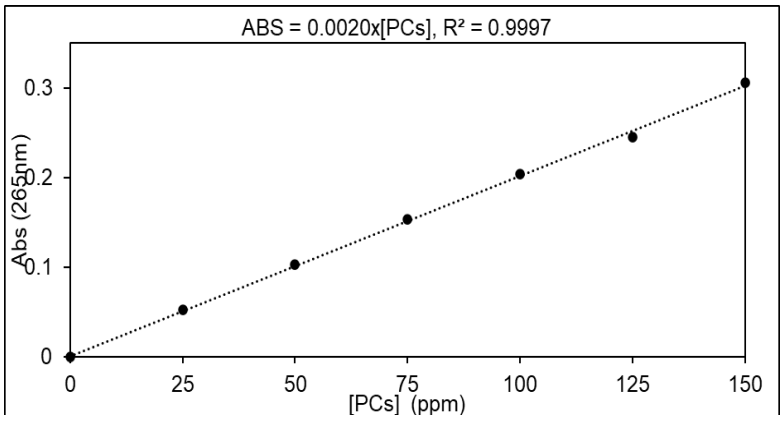

Figure 49- Us-Vis spectroscopy Calibration curve with following solutions of P-cresyl : 25 ppm, 50 ppm, 75 ppm, 100 ppm, 125 ppm and 150 ppm. Regression line given by: Absorbance (ABS)=0.002×[PCs](in ppm),(Absorbance measure in 265nm) with the respective coefficient of correlation, R2=0.9995.

Appendix C.2- Calibration curve of Urea 200-1000ppm

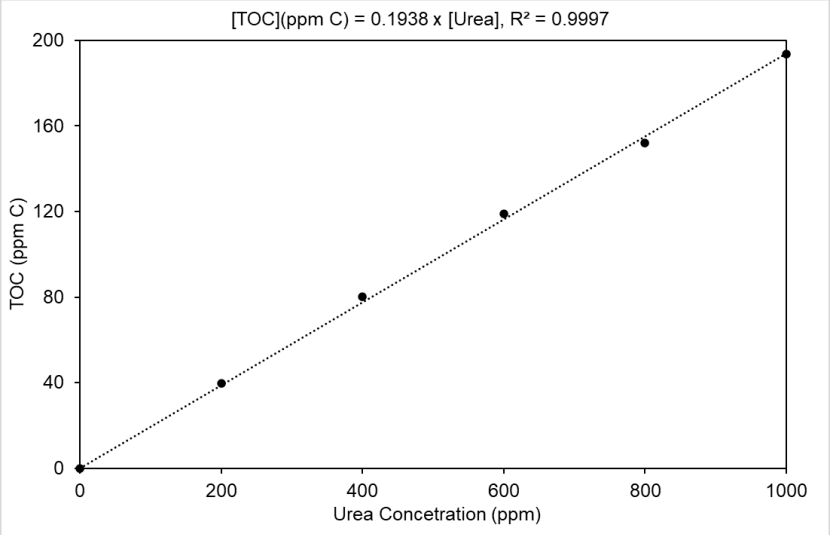

Figure 50- TOC calibration curve with solutions of Urea: 200 ppm, 400 ppm, 600 ppm, 800 ppm, 1000 ppm, with regression line given by: [TOC](in ppm of Carbon)=0.1938×[Urea](in ppm), and respective coefficient of correlation, Rr=0.9997.

Appendix C.3- Calibration curve of Urea 500-3000ppm

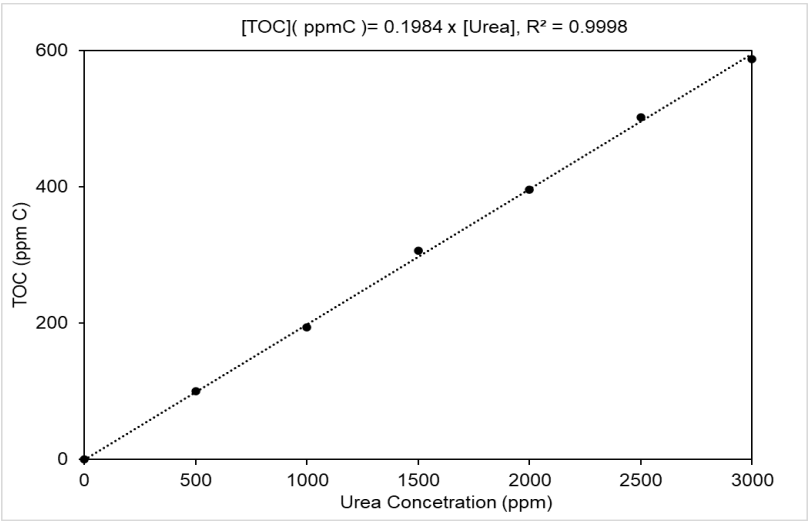

Figure 51- TOC calibration curve with solutions of Urea: 500 ppm, 1000 ppm, 1500 ppm, 2000 ppm, 2500 ppm and 3000 ppm, with regression line given by: [TOC](in ppm of Carbon)=0.1984×[Urea](in ppm), and respective coefficient of correlation, Rr=0.9998.

Appendix D- Mass Flux Permeability of Uremic toxins: Urea, PCs and Pcs+Albumin(BSA)

Table 15- Mass flux permeability (Jp) of Kg/h.m2 of each membrane to 400 ppm of Urea solution at transmembrane pressure (ΔP_t) of : 0.5,1,2,3 bar.

ΔPt/Membrane	Permeate flux (Jp)(Kg/m².h) 400 ppm Urea				
	CA	CA_UiO66	CA/SiO_2_UiO66	CA/SiO_2	CA/SiO_2__G20
0.5	3.7	1.5	11.5	2.8	0.8
1	8.5	2.0	17.1	4.4	2.0
2	18.1	4.4	34.1	11.0	4.0
3	29.5	8.3	69.9	17.3	6.9

Table 16- Mass flux permeability (Jp) of Kg/h.m2 of each membrane to 4600 ppm of Urea solution at transmembrane pressure (ΔP_t) of : 0.5,1,2,3 bar.

ΔPt/Membrane	Permeate flux (Jp)(Kg/m².h) 4600 ppm of Urea				
	CA	CA_UiO66	CA/SiO_2_UiO66	CA/SiO_2	CA/SiO_2_G20
0.5	4.9	1.2	10.2	2.3	0.7
1	8.7	1.9	18.2	4.3	1.5
2	21.2	5.5	53.8	12.5	4.6
3	28.7	7.0	68.5	17.2	5.5

Table 17- Mass flux permeability (Jp) of Kg/h.m2 of each membrane to 100 ppm of PCs solution at transmembrane pressure (ΔP_t) of : 0.5,1,2,3 bar.

ΔPt/Membrane	Permeate flux (Jp)(Kg/m².h) 100 ppm of PCs				
	CA	CA_UiO66	CA/SiO_2_UIO66	CA/SiO_2	CA/SiO_2_G20
0.5	4.9	1.1	7.5	2.3	0.8
1	7.4	1.9	16.9	4.1	1.5
2	17.8	5	41.9	10.8	3.9
3	31.0	9	73.9	18.8	7.5

Table 18- Mass flux permeability (Jp) of Kg/h.m2 of each membrane to 100 ppm of PCs solution at transmembrane pressure (ΔP_t) of : 0.5,1,2,3 bar.

ΔPt/Membrane	Permeate flux (Jp)(Kg/m².h) 100 ppm of PCs + 500 ppm of BSA				
	CA	CA_UiO66	CA/SiO_2_UiO66	CA/SiO_2	CA/SiO_2_G20
0.5	5.30	0.94	11.87	1.94	0.83
1	3.96	0.95	12.32	2.45	0.84
2	8.25	4.30	52.25	10.29	2.37
3	10.13	7.09	73.12	14.54	4.45

Appendix E: Fitting HN parameters and temperature interval of each process

Table 19- Fitting parameters α_{HN}, β_{HN} and T range for CA/SiO_2, CA_UiO66 and CA/SiO_2_UiO66 membranes

	CA/SiO_2			CA_UiO66			CA/SiO_2_UiO66		
	Process 0	Process 1	Process 2	Process 0	Process 1	Process 2	Process 0	Process 1	Process 2
α_{HN}	0.36	0.7	0.8	0.69	0.4	0.63	0.7	0.4	0.7
β_{HN}	0.7	1	1	1	0.73	1	1	0.5	1
ΔT (°C)	[-110,-75]	[-110,0]	[-55,5]	[-120,5]	[-120,-85]	[-60,5]	[-120,-5]	[-120,-90]	[-60,-5]

Table 20- Fitting parameters α_{HN}, β_{HN} and T range of CA_G20 and CA/SiO_2_G20 membranes.

	CA_G20			CA/SiO_2_G20			
	Process 1	Process 2	Process 3	Process 0	Process 1	Process 2	Process 3
α_{HN}	0.56	0.51	0.6	0.36	0.7	0.76	0.7
β_{HN}	0.65	1	1	0.7	1	1	1
T range **(°C)**	[-110,-15]	[-110,-75]	[-80,25]	[-110,-70]	[-110,-70]	[-75,5]	[-70,55]

Table 21- Fitting parameters α_{HN}, β_{HN} and T range of CA_GT and CA/SiO_2_GT membranes.

	CA_GT					CA/SiO_2_GT		
	Process 0	Process 1	Process 2	Process 3	Process 4	Process 0	Process 1	Process 2
α_{HN}	0.5	0.5	0.47	0.7	0.6	0.5	0.4	0.5
β_{HN}	1	0.7	1	1	1	1	0.4	1
T range (°C)	[-110,-75]	[-80,10]	[-105,-70]	[-80,40]	[-30,40]	[-115,-70]	[-110,-95]	[-75,5]

Appendix F

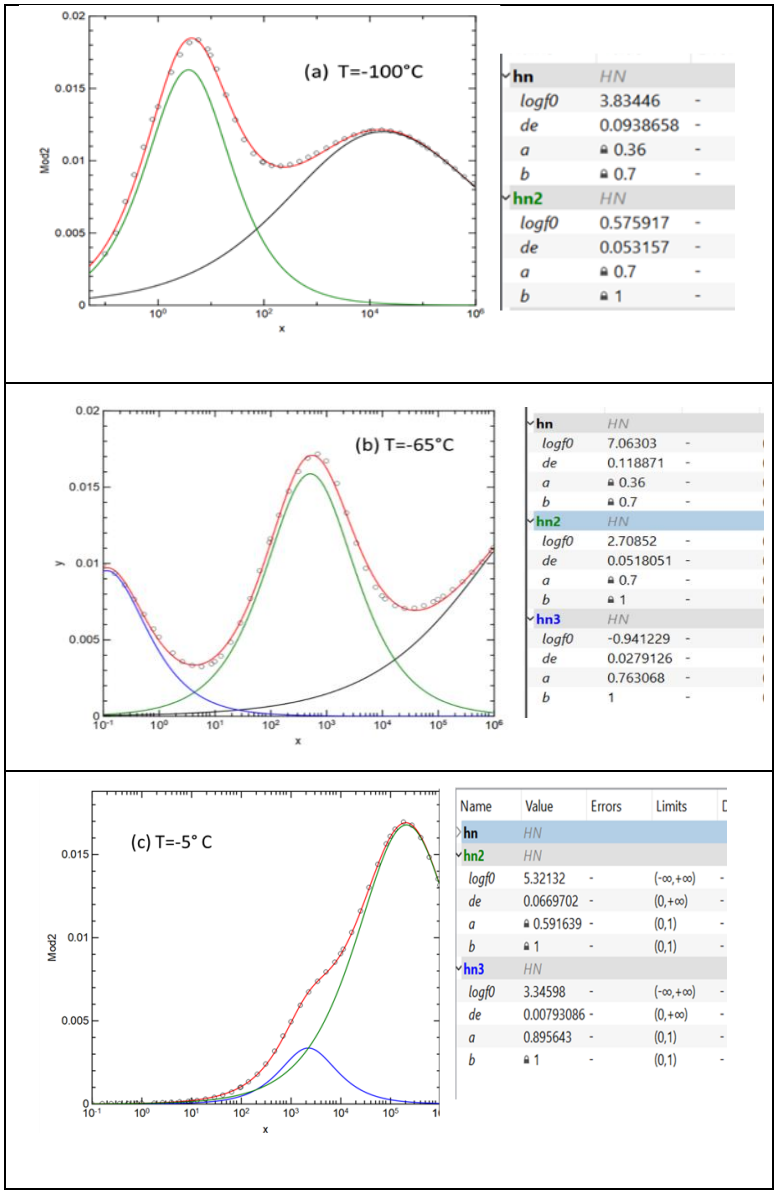

Figure 52- Isothermal data collected at -100(a), -65(b) and -5 °C(c). The individual HN fitting functions used are blue and green lines, and the overall fit is depicted as red line and with the corresponding parameters of HN function for CA/SiO_2 membrane.

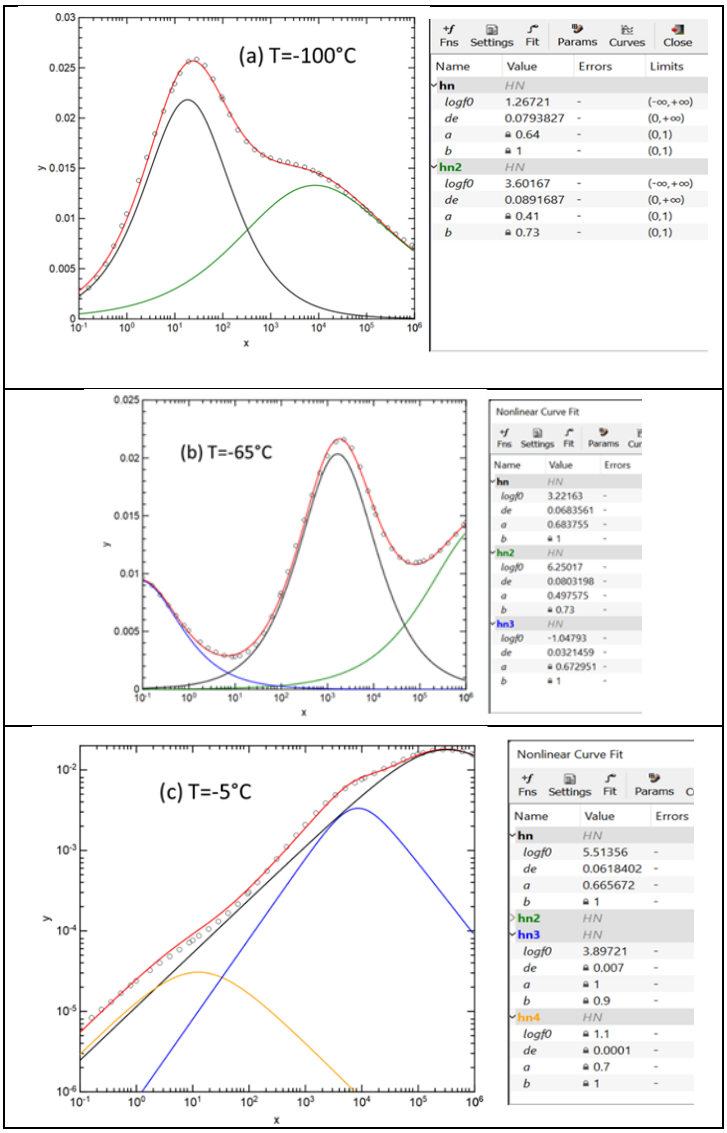

Figure 53- Isothermal data collected at -100(a), -65(b) and -5 °C(c). The individual HN fitting functions used are blue and green lines, and the overall fit is depicted as red line and with the corresponding parameters of HN function for CA/SiO_2_UiO66 membrane.